

Optical Waveguides for Sensing Applications

**Thesis submitted in partial fulfillment
of the requirements for the degree of
“DOCTOR OF PHILOSOPHY”**

by

Aviad

Katiyi

**Submitted to the Senate of Ben-Gurion University
of the Negev**

25/10/2021

Beer-Sheva

Optical Waveguides for Sensing Applications

**Thesis submitted in partial fulfillment
of the requirements for the degree of
“DOCTOR OF PHILOSOPHY”**

by

Aviad

Katiyi

**Submitted to the Senate of Ben-Gurion University
of the Negev**

Approved by the advisor 

Approved by the Dean of the Kreitman School of Advanced Graduate Studies

25/10/2021

Beer-Sheva

This work was carried out under the supervision of
Prof. Alina karabchevsky

In the Department Electro-Optics and Photonics Engineering

Faculty Engineering Sciences

Research-Student's Affidavit when Submitting the Doctoral Thesis for Judgment

I Aviad Katiyi, whose signature appears below, hereby declare that
(Please mark the appropriate statements):

I have written this Thesis by myself, except for the help and guidance offered by my Thesis Advisors.

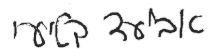
The scientific materials included in this Thesis are products of my own research, culled from the period during which I was a research student.

This Thesis incorporates research materials produced in cooperation with others, excluding the technical help, excluding result analysis, commonly applied during such experimental work. Therefore, I attach an additional affidavit stating the contributions made by myself and the other participants in this research, which has been approved by them and submitted with their approval.

This thesis is in Manuscript Format, includes one or more papers in which I am an "equal contributor". I therefore attach an additional affidavit signed by other equal contributor(s) stating their contribution to the paper and their approval that that paper could not be included in another Manuscript Format Thesis.

Date: 25/10/2021

Student's name: Aviad Katiyi

Signature: 

Abstract

Guided wave optics provides a rich platform for fundamental investigations and applied research in a variety of systems. This is due to the fact that waveguides possess unique features, such as a large evanescent field, compactness and, most importantly, their ability to be configured according to the required application. The ability to probe molecular fundamental or overtone vibrations is fundamental to healthcare monitoring techniques and sensing, since it provides information about the molecular structure. Overtone vibrational spectroscopy is based on the interaction between light and matter and is a powerful tool for investigating molecular structures in affordable near-infrared. However, the near-IR region, which exhibits great potential, has not been investigated properly - due to the low absorption cross-section of the overtone vibrational transitions. Understanding the absorption mechanism of molecular vibrational overtone transitions will enable the development of new, efficient and affordable detection methods, which can be used for a variety of applications such as chemical sensors and medical applications, and even for the monitoring efficiency of cancer treatment. To close this gap, during my Ph.D. research I explored the overtone transitions in several systems, including the different molecules and different waveguide architectures detailed in this thesis.

My research focuses on the study of the absorption mechanism by molecular vibrational overtone transitions with guided wave optic architectures. I found that optical waveguides can be utilized for overtone spectroscopy. By creating disturbances/perturbations in the guiding layer, such as holes or gratings, the sensitivity can be increased. In addition, decreasing the confinement of the mode by tapering a fiber can be also used to enhance the sensitivity, due to an increase in the evanescent field penetration depth.

Table of Contents

1	Introduction	5
1.1	State of the art	5
1.2	Methods	7
1.2.1	Optical guided wave structure	7
1.2.2	Vibrational spectroscopy	10
1.2.3	Numerical simulation	14
1.2.4	Experimental setup	15
1.2.5	The fabrication process of microfibers	16
1.2.6	Focused Ion Beam (FIB) technique	17
2	Published papers	19
2.1	Si Nanostrip Optical Waveguide for On-Chip Broadband Molecular Overtone Spectroscopy in Near-Infrared	19
2.2	Deflected Talbot-Mediated Overtone Spectroscopy in Near-Infrared as a Label-Free Sensor on a Chip	26
2.3	Surface roughness-induced absorption acts as an ovarian cancer cells growth sensor-monitor	33
3	Additional studies	41
3.1	Scattering pattern of a cylindrical inclusion on a waveguide	41
3.2	Subwavelength grating on a waveguide for enhanced sensitivity	42
4	Conclusions and Discussion	46
4.1	Future research and perspectives	47

List of Figures

1	Cross-section of common optical waveguide configurations: (a) ridge waveguide, (b) slot waveguide, (c) rib waveguide, (d) buried waveguide and (e) diffused waveguide.	6
2	(a) Slab waveguide configuration. (b) Illustration of the light properties for different order modes [29].	7
3	The possible modes in a planar waveguide [30].	9
4	Diagrams of an oscillator mechanism [32] described by the energy levels (top) and the corresponding spectral transmittance patterns (bottom) for: (a) Harmonic oscillator, (b) harmonic oscillator with the heterogeneity of the medium and (c) anharmonic oscillator. D_e and r_e are the dissociation energy and the equilibrium bond distance, respectively.	11
5	Illustration of Morse potential function for anharmonic vibration compared to potential function for harmonic vibration. E_f - fundamental vibrational transition energy. E_{oi} - i^{th} overtone vibrational transition energy. D_e - is the dissociation energy.	13
6	Schemes of the numerical simulation methods: (a) Yee scheme for finite difference time domain (FDTD) method [34] and (b) finite element method (FEM) scheme [35].	15
7	(a) The coupling setup of laser to fiber. (b) The waveguide input and output coupling setup.	16
8	(a) Illustration of a tapered fiber. (b) Illustration of the tapering machine [36].	17
9	Illustration of a FIB-SEM dual-beam with a zoom of the electrons and ion beam interaction with the sample [37].	17
10	Illustration of the waveguide with cylindrical inclusion through the guiding layer [51].	41
11	Angular diagrams for $D = \lambda/(5, 10, 20, 100)$ (different diameter from each column as labeled above the columns) for fundamental TE. Some of the fields at xy plane in the polar graph are multiplied by 10 for comparison. The blue curve shows the angular diagram in yz plane and the red curve shows the angular diagram in xy plane, respectively. The 1 st row shows the electric dipole (eDip), the 2 nd row shows the magnetic dipole (mDip), and the 3 rd row shows the electric quadrupole (eQuad) - as labeled in the y-axis of (a,e,i) (adapted from [51]).	42

12	Calculated magnetic dipole for $D = \lambda/(5, 10, 20, 50, 100)$ presented in Cartesian coordinates plot (adapted from [51]).	43
13	Illustration of the waveguide with the subwavelength grating.	43
14	The normalized electric field of the fundamental transverse electric (TE) mode in distance of 50 nm from the top facet for (a) untouched rib silicon waveguide and (b) rib silicon waveguide with subwavelength grating.	44
15	Scanning electron microscope (SEM) image of the fabricated subwavelength grating on the waveguide.	44
16	(a) Laser to waveguide coupling setup. (b) Scattering from the grating. (c) The measured transmission of a clean untouched waveguide (black curve), untouched waveguide with <i>N</i> -Methylaniline (blue curve) and waveguide with milled subwavelength grating and <i>N</i> -Methylaniline (red curve). (d) Transmission of <i>N</i> -Methylaniline in 1 cm cuvette.	45

Abstract

Guided wave optics provides a rich platform for fundamental investigations and applied research in a variety of systems. This is due to the fact that waveguides possess unique features, such as a large evanescent field, compactness and, most importantly, their ability to be configured according to the required application. The ability to probe molecular fundamental or overtone vibrations is fundamental to healthcare monitoring techniques and sensing, since it provides information about the molecular structure. Overtone vibrational spectroscopy is based on the interaction between light and matter and is a powerful tool for investigating molecular structures in affordable near-infrared. However, the near-IR region, which exhibits great potential, has not been investigated properly - due to the low absorption cross-section of the overtone vibrational transitions. Understanding the absorption mechanism of molecular vibrational overtone transitions will enable the development of new, efficient and affordable detection methods, which can be used for a variety of applications such as chemical sensors and medical applications, and even for the monitoring efficiency of cancer treatment. To close this gap, during my Ph.D. research I explored the overtone transitions in several systems, including the different molecules and different waveguide architectures detailed in this thesis.

My research focuses on the study of the absorption mechanism by molecular vibrational overtone transitions with guided wave optic architectures. I found that optical waveguides can be utilized for overtone spectroscopy. By creating disturbances/perturbations in the guiding layer, such as holes or gratings, the sensitivity can be increased. In addition, decreasing the confinement of the mode by tapering a fiber can be also used to enhance the sensitivity, due to an increase in the evanescent field penetration depth.

1 Introduction

1.1 State of the art

Integrated photonics is a branch of photonics in which planar dielectric waveguides are fabricated on a chip, such as those summarized in ref. [1]. On-chip nanophotonics is an emerging and rapidly growing branch of integrated photonics in which the optical waveguides have nanoscale dimensions. Due to their small dimensions, waveguides allow miniaturization and design of efficient optical components on a chip [2]. The material on which the photonic integrated circuitry (PIC) is made dictates its functionality. It dictates the operating wavelengths and applications in terms of passive or active functionality. The materials for waveguides are divided into two groups: passive and active materials. Passive materials are materials that transmit light without absorption, generation or modulation of light. The first passive material offered for guiding light was glass. It is dated back to 1880 when William Wheeler transmitted light through a glass 'light pipe'. In 1966, a circular fiber was first used as a guiding medium for light transmission [3]. In 1976 silicon was used for the first time for optical waveguides. In the early 1990s, a silicon-on-insulator (SOI) wafer, originally used for electronics, was first used for an optical waveguide [4, 5]. This progress opened the field of photonic integrated circuits, due to the well-understood and robust material previously used in the electronics industry. The development of optics communication gave rise to the development of active materials for modulating and amplifying guided light. The first proposed material was lithium niobate (LiNbO_3), a human-made ferroelectric crystalline material with a large electro-optic effect [6] that allows its utilization for optical modulators [7, 8]. Due to the evolution in the field of integrated photonics, the need for active materials that can generate light has grown. Semiconductors have a direct bandgap that can be used for light generation on a chip [9]. Furthermore, active materials can be used for the fabrication of detectors on a chip [10]. Therefore, choosing the right material for the waveguide is crucial.

Optical waveguides are becoming an attractive building block in a variety of systems due to their unique features such as large evanescent field, compactness and, mostly, the ability to be configured to the required application. Waveguides used in integrated photonics are planar and composed of at least three layers: the substrate, the guiding layer (or core), and a cladding (air or others). The light is guided in the waveguide due to total internal reflection (TIR) [11]. Common configurations of waveguides [1] include slab, strip loaded, ridge, rib, buried and diffused, as shown in Fig. 1. Each configuration has properties that can be utilized for different applications. For example, a ridge waveguide can be used for sensing due to the large evanescent field, while a buried waveguide configuration can be used for optics communication. Optical waveguides can be used for both passive and active

applications such as splitters [12, 13], directional couplers [14, 15], optical modulators [16, 17] and light sources [18, 19].

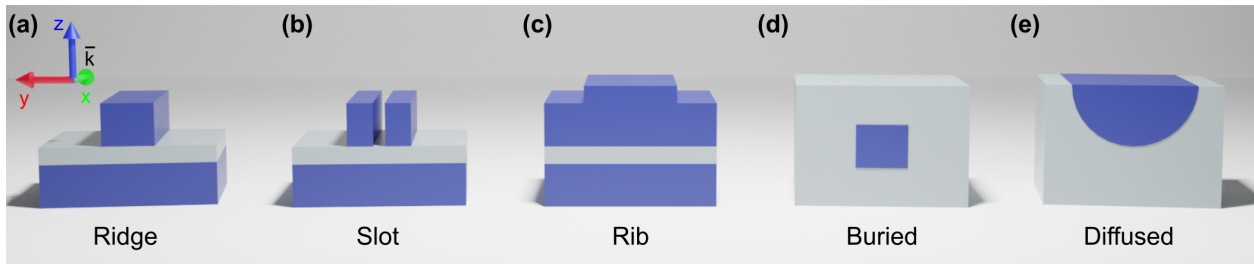


Figure 1: Cross-section of common optical waveguide configurations: (a) ridge waveguide, (b) slot waveguide, (c) rib waveguide, (d) buried waveguide and (e) diffused waveguide.

Optical waveguides can be also used for spectroscopy. Spectroscopy focuses on the interaction between radiation and matter [20] and can be used for remote and on-site detection. For example, when illuminated with infrared (IR) radiation, the atoms in the molecule start to vibrate. Each atom bond vibrates in different modes, resulting in distinct absorption bands for different atom bonds that give information about the molecule structure. Refractometers are sensors that rely on changes in the refractive index of the analyte in a specific wavelength [21, 22]. Refractometers can achieve high sensitivity for a refractive index change with a resolution of 5.4×10^{-5} [21]. However, they lack the ability to identify analytes whose refractive indices resemble other materials.

Another spectroscopic method is based on evanescent field absorption. Along the propagation, a fraction of the field in a guided mode can penetrate beyond the guiding layer and exponentially decay. This fraction of the field is called the evanescent field. Guided wave structures can be used for an evanescent field sensor, which is also named 'attenuated total reflection' (ATR) sensor. It is based on the interaction between the evanescent field and the analyte. It requires little or no sample preparation. In addition, ATR is good for highly absorptive samples [23] due to the small penetration depth of the evanescent field. A ring-resonator can be used as an evanescent field sensor [24]. It exhibits enhanced sensitivity due to the strong influence of the resonator environment. It can sense temperature, refractive index, and even strain. The sensitivity of the sensor is defined by the wavelength distance between two resonances (FSR - free spectral range). Using a microring resonator, the spectra of *N*-methylaniline (NMA) from 1.46 to 1.6 μm can be identified with a resolution of 1 nm [25]. However, it cannot provide broadband sensing, due to limitations of the FSR-based method [25]. Another option is the use of glass waveguides. Glass waveguides can be used for molecular overtones in near-infrared while integrated with a microfluidic chip [26]. In addition, diffused waveguides were used to detect N-H bond overtone absorption around 1.5

μm [27]. The waveguides were pretreated by negative charge using plasma oxygen, which is not suitable for on-site long-time measurements. Recently, optical waveguides were proposed for detecting gas. The slow light phenomenon in a subwavelength grating waveguide was utilized for enhancing the absorption of methane on a chip [28].

1.2 Methods

1.2.1 Optical guided wave structure

My work focused on the study of wave structures. The propagation of light in a waveguide is based on a total internal reflection. When light hits the boundary between high to low index material at a specific angle, called the critical angle, the light will be fully reflected. This phenomenon is called total internal reflection. Therefore, for enabling the propagation of light inside the waveguide, the refractive index of the guiding layer in a waveguide structure needs to be higher than its surroundings. For the understanding of optical waveguide behavior, a basic waveguide composed of three layers - a substrate, a guiding layer and a superstrate - will be analyzed in this section, as illustrated in Fig. 2a. This configuration is called a slab waveguide. This structure is not practical due to its infinite width but can be used for basic analysis of waveguide modes and behavior. Figure 2b illustrates the differences between the properties of different order modes. Each mode has a different reflection angle. As the order of the mode increases, the reflection angle and the propagation constant (β) decreases.

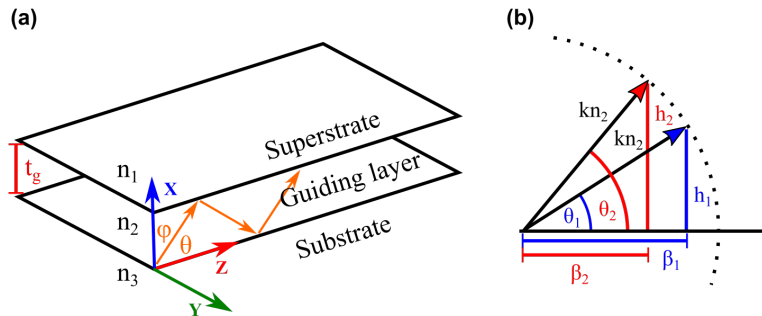


Figure 2: (a) Slab waveguide configuration. (b) Illustration of the light properties for different order modes [29].

The optical wave propagates in the waveguide as a mode. Mode is the spatial distribution of optical energy propagating inside the waveguide and constant in time. The mode can be described as a solution of Maxwell's wave equation

$$\nabla^2 \vec{E}(\vec{r}, t) = \frac{n^2(\vec{r})}{c^2} \frac{\partial^2 \vec{E}(\vec{r}, t)}{\partial t^2} \quad (1)$$

where E is the electric field, \vec{r} is the radius vector, n is the refractive index and c is the light speed in vacuum. Assuming monochromatic light, the solution is of the form

$$\vec{E}(\vec{r}, t) = \vec{E}(\vec{r})e^{j\omega t} \quad (2)$$

and we obtain

$$[\nabla^2 + k^2 n(\vec{r})^2] \vec{E}(\vec{r}, t) = 0 \quad (3)$$

where $k = \omega/c$ is the wavenumber and ω is the angular frequency.

Assuming the dimensions of the slab waveguide with infinite width in y axis (as shown in Fig. 2a) and a uniform plane wave, $\vec{E}(\vec{r}) = \vec{E}(x, y) \exp(-j\beta z)$, we get the following equation:

$$\partial^2 E(x, y) / \partial x^2 + (k^2 n_i^2 - \beta^2) E(x, y) = 0 \quad (4)$$

where $E(x, y)$ is one of the cartesian components of $\vec{E}(x, y)$, i is the layer number and β is the propagation constant. For each mode, there is a corresponding propagation constant β_m that is given by:

$$\beta_m = kn_2 \sin \phi_m = kn_2 \cos \theta_m \quad (5)$$

where m is the number of the mode, and ϕ and θ is the reflection and propagation angle, respectively (Fig. 2b).

Due to the different propagation angles, each mode has a different velocity and, therefore, a different effective index for the guiding material. The effective index for a mode m is given as:

$$n_{\text{eff},m} = c/v_m = \beta_m/k \quad (6)$$

As can be seen from Eq. (4), the mode formation is dependent on the propagation constant and, therefore, on the mode effective index. Figure 3 shows the possible modes that exist in an optical waveguide as a function of the mode effective refractive index. There are three possible scenarios. First, when the effective index of the mode is smaller than the index of the superstrate (green bar region), the mode is air radiation mode and is not propagating. Second, when the effective index of the mode is lower than the index of the substrate and higher than the index of the superstrate (red bar region), the mode is substrate radiation mode and is propagating for a very short distance. Third, when the effective mode index is lower than the refractive index of the guiding layer and higher than the refractive index of the substrate (blue bar region), the mode is guided mode and is propagating in the waveguide. Therefore, there are only a limited number of guided modes that can exist when

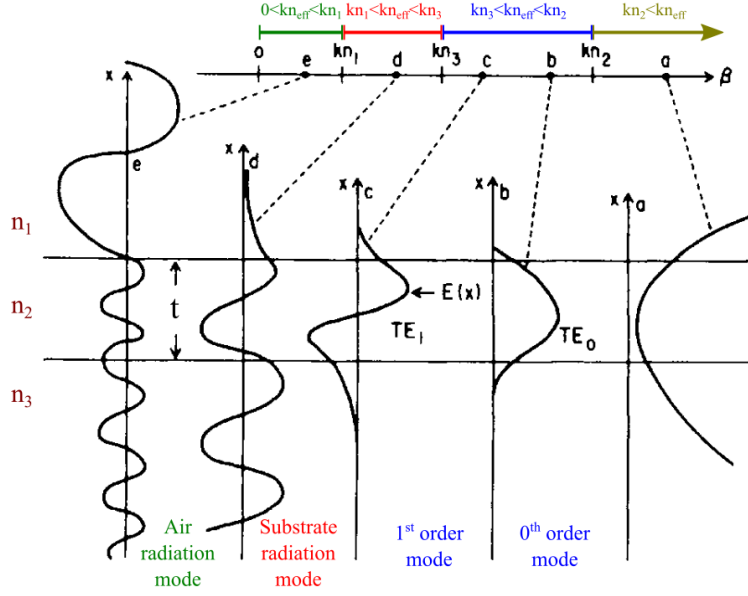


Figure 3: The possible modes in a planar waveguide [30].

the mode effective refractive index is in the range

$$n_3 \leq n_{\text{eff}} \leq n_2 \quad (7)$$

Solving Eq. (4) for the effective refractive index range for guided modes gives the following solutions for a slab waveguide for each region as:

$$E(x) = \begin{cases} Ae^{-q(x-t_g)} & t_g < x < \infty \\ B \cos(hx) + C \sin(hx) & 0 \leq x \leq t_g \\ De^{px} & -\infty < x < 0 \end{cases} \quad (8)$$

$$\begin{aligned} q &= \sqrt{\beta^2 - k^2 n_1^2} \\ h &= \sqrt{k^2 n_2^2 - \beta^2} \\ p &= \sqrt{\beta^2 - k^2 n_3^2} \end{aligned} \quad (9)$$

where t_g is the guiding layer thickness and A , B , C , and D are defined from the boundary conditions.

As can be seen from the solutions outside the guiding layer, a fraction of the field in a guided mode can penetrate beyond the guiding layer and exponentially decay. This is called the evanescent field. It interacts with its surrounding and can be utilized for sensing applications. The penetration depth of the evanescent field to a medium outside the guiding

layer is defined as:

$$d_p = \frac{\lambda}{2\pi\sqrt{n_g^2 \sin^2(\phi_i) - n_a^2}} \quad (10)$$

where n_a is the refractive index for the medium, n_g is the refractive index for the guiding medium and ϕ_i is the incident angle inside the guiding layer as illustrated in Fig. 2a. Equation (10) shows that the smaller the incident angle, the larger the penetration depth of the evanescent field into the medium. The penetration depth depends on the incident angle, that in turn depends on the effective mode index as shown in Eq. (11).

$$\phi_{i,m} = \sin^{-1}(n_{\text{eff},m}/n_g) \quad (11)$$

Equations (10) and (11) show that as the effective index of the mode is reduced, the penetration depth of the evanescent field increases and the mode is less confined in the guiding layer. Therefore, decreasing the effective refractive index, which can be achieved by decreasing the dimensions of the guiding layer or coupling power to higher-order modes, can be used for enhancing the evanescent field and improving sensitivity.

1.2.2 Vibrational spectroscopy

My work included the study of guided wave optics structures for broadband label-free overtone spectroscopy in the near-infrared (NIR). In the infrared (IR) region, the interaction between the radiation and the molecule causes the atoms to vibrate. Each molecule can have a different number of vibrational modes with different energies. Each transition between vibrational modes has a different probability to occur. The rate of transitions can be defined by Einstein coefficient of stimulated absorption as [31]

$$B = \frac{|\boldsymbol{\mu}_{ij}|^2}{6\varepsilon_0\hbar^2} \quad (12)$$

where ε_0 is the permittivity of free space, \hbar is the reduced Planck constant and $\boldsymbol{\mu}_{ij}$ is the electric dipole transition moment from state i to state j which is defined as

$$\boldsymbol{\mu}_{ij} = \langle i|\boldsymbol{\mu}|j \rangle = \int \psi_i^* \boldsymbol{\mu} \psi_j dr \quad (13)$$

where ψ is the wave function and $\boldsymbol{\mu}$ is the electric dipole moment, defined as

$$\boldsymbol{\mu} = \boldsymbol{\mu}_0 + \left(\frac{\partial \boldsymbol{\mu}}{\partial r}\right)_0 r + \frac{1}{2} \left(\frac{\partial^2 \boldsymbol{\mu}}{\partial r^2}\right)_0 r^2 + \dots \quad (14)$$

where $\boldsymbol{\mu}_0$ is the equilibrium value of the dipole moment, 0 is the value in the equilibrium and r is the displacement.

Inserting Eq. (14) into Eq. (13), the following is obtained:

$$\langle i|\boldsymbol{\mu}|j\rangle = \boldsymbol{\mu}_0 \langle i|j\rangle + \left(\frac{\partial\boldsymbol{\mu}}{\partial r}\right)_0 \langle i|r|j\rangle + \frac{1}{2}\left(\frac{\partial^2\boldsymbol{\mu}}{\partial r^2}\right)_0 \langle i|r^2|j\rangle + \dots$$

The states are orthogonal and the transition moment is defined as

$$\langle i|\boldsymbol{\mu}|j\rangle = \left(\frac{\partial\boldsymbol{\mu}}{\partial r}\right)_0 \langle i|r|j\rangle + \frac{1}{2}\left(\frac{\partial^2\boldsymbol{\mu}}{\partial r^2}\right)_0 \langle i|r^2|j\rangle + \dots \quad (15)$$

The transition matrix is non-zero only when there is a change in the dipole moment during the vibration. Therefore, the selection rule for IR absorption is that a photon can be absorbed only when a change in the dipole moment occurs during the vibration.

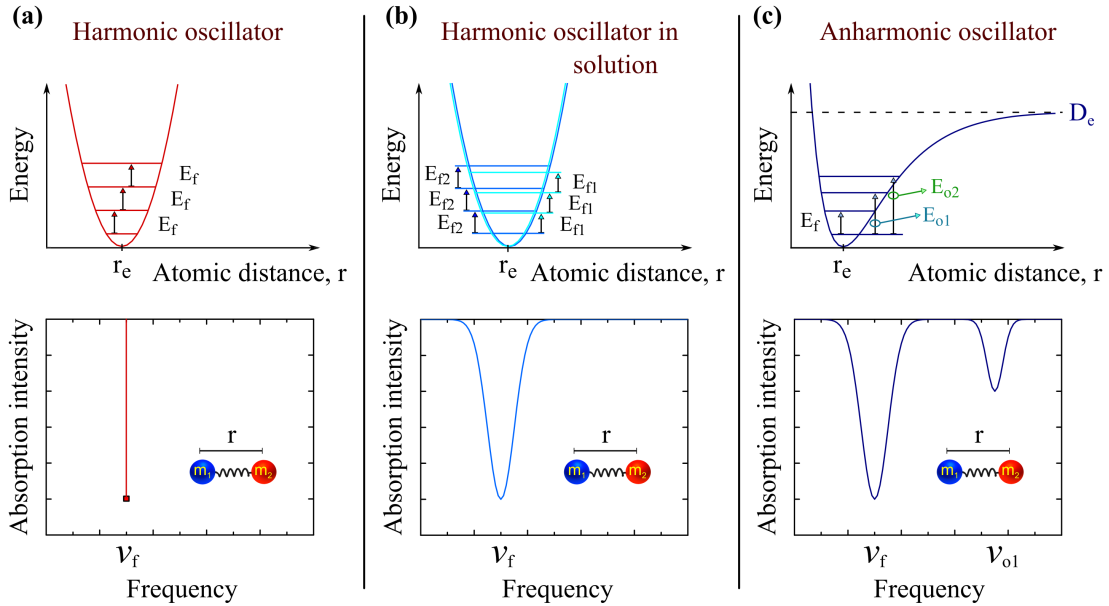


Figure 4: Diagrams of an oscillator mechanism [32] described by the energy levels (top) and the corresponding spectral transmittance patterns (bottom) for: (a) Harmonic oscillator, (b) harmonic oscillator with the heterogeneity of the medium and (c) anharmonic oscillator. D_e and r_e are the dissociation energy and the equilibrium bond distance, respectively.

The first proposed model for the vibration of a molecule was a model of a harmonic oscillator in which the vibration is described as that of a spring. For calculating the vibrational energy levels of the molecule, the time-independent Schrödinger equation for a single particle

can be used, defined as:

$$E\psi = H\psi = (T + V)\psi = -\frac{\hbar^2}{2m}\nabla^2\psi + V(r)\psi \quad (16)$$

where E is the total energy, m is the mass, $V(r)$ is the potential energy, H is the Hamiltonian, which is the operator for the total energy of a system, and T and V are the operators for the kinetic and the potential energy, respectively.

The Schrödinger equation for a movement in one dimension, which fits the harmonic model, is defined as:

$$E\psi = -\frac{\hbar^2}{2m}\frac{d^2\psi}{dx^2} + V(x)\psi \quad (17)$$

In the harmonic model, the potential energy is parabolic, as shown in Fig. 4a (top). By solving the Schrödinger equation for a parabolic potential function, the energy levels of a harmonic oscillator are calculated as [31]:

$$E_v = \left(v + \frac{1}{2}\right)\hbar\omega \quad (18)$$

$$\omega = \sqrt{\frac{k}{M}} \quad M = \frac{m_1 \cdot m_2}{m_1 + m_2} \quad (19)$$

where v is the number of the energy level, k is the force constant, M is the reduced mass and ω is the natural angular frequency of the oscillator.

Assuming a small displacement, the dipole moment is changed linearly along with the vibration. Therefore, the second and higher-order derivatives of the dipole moment, defined by Eq. (14), are neglected, and the electric dipole transition moment is defined as:

$$\mu_{ij} = \langle i|\mu|j \rangle = \left(\frac{\partial\mu}{\partial r}\right)_0 \langle i|r|j \rangle \quad (20)$$

Assuming the harmonic oscillator model, the wavefunctions are Hermite polynomials and, as a result, non-zero contributions will be obtained only when $v' = v + 1$ [31]. Therefore, the selection rule allows only a transition of $\Delta v = \pm 1$. This means that only a photon with specific energy corresponding to a specific frequency, called the fundamental frequency, can be absorbed, resulting in fundamental vibration. The absorption of a photon with specific energy causes a discrete absorption with zero line width, as illustrated in Fig. 4a. Practically, the molecules are in a heterogeneous solution that has a different influence on each molecule.

The heterogeneous solution results in a small change in the energy levels for each molecule, therefore the absorption band experiences a broadening effect, as illustrated in Fig. 4b.

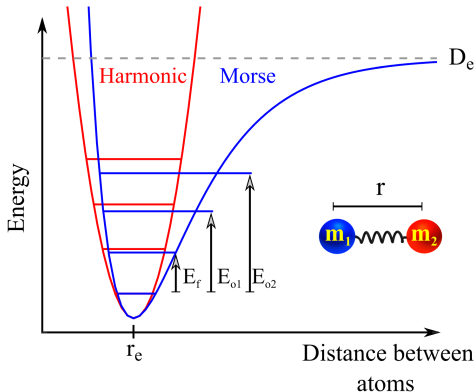


Figure 5: Illustration of Morse potential function for anharmonic vibration compared to potential function for harmonic vibration. E_f - fundamental vibrational transition energy. E_{oi} - i^{th} overtone vibrational transition energy. D_e - is the dissociation energy.

In practice, the molecule has electrical and mechanical anharmonicity that causes the molecule to behave as an anharmonic oscillator. An estimated model for an anharmonic oscillator is the Morse potential function. Morse potential function, in contrast to the harmonic model, includes the effect of bond breaking D_e and the anharmonicity of the bonds. These differences can be seen in Fig. 5. The Morse potential function is defined as:

$$E(r) = V(r) = D_e(1 - \exp[-a(r - r_e)])^2 \quad (21)$$

where D_e is the dissociation energy, a is a constant for a particular molecule, r is the distance between atoms and r_e is the equilibrium bond distance.

Solving the Schrödinger equation for the Morse potential gives the energy levels for the anharmonic model as [31]:

$$E_v = (v + 1/2)\hbar\omega - (v + 1/2)^2\chi_e\hbar\omega \quad (22)$$

where v is the number of the energy level, \hbar is the reduced Planck constant and χ_e is the anharmonicity coefficient.

Due to the anharmonicity of the molecule, the higher-order derivatives in the dipole moment in Eq. (14) are non-zero and, therefore, cannot be neglected. As a result, the transition moment is defined as Eq. (15). However, in polyatomic molecules, the vibration affects other bonds and the restoring force. Instead of using the displacement r , we define Q ,

which is the linear combination of the displacements. For example, for a symmetric stretch of CO₂, the linear combination of the displacements Q is defined as:

$$Q = \frac{1}{\sqrt{2}}(q_1 - q_3) \quad (23)$$

where q is the mass-weighted coordinates, defined as:

$$q_i = \sqrt{m_i}r_i \quad (24)$$

Using the new definition of the displacement (shown in Eq. (23)), the dipole moment of a diatomic molecule is defined as:

$$\boldsymbol{\mu} = \boldsymbol{\mu}_0 + \sum_i \left(\frac{\partial \boldsymbol{\mu}}{\partial Q_i} \right)_0 Q_i + \frac{1}{2} \sum_{i,j} \left(\frac{\partial^2 \boldsymbol{\mu}}{\partial Q_i \partial Q_j} \right)_0 Q_i Q_j + \dots \quad (25)$$

Due to the anharmonicity, the probability of transitions of $\Delta v > 1$ (for example: 0→2, 0→3 and 0→4) is non-zero and the transitions are allowed. The transition of $\Delta v > 1$ is called overtone. The vibrational overtone transitions result in multiple absorption bands, as illustrated in Fig. 4c. In addition, in polyatomic molecules, when $i \neq j$ in Eq. (25), two vibrational modes are excited simultaneously. The excitation of two modes is called the combination mode. For example, in aniline, the combination modes cause a broadening around the N-H first overtone absorption at 1.5 μm [33]. Another phenomenon that occurs in the anharmonic oscillator model is the absorption broadening caused by a transition from an excited state. Eq. (22) shows that as energy increases, the difference between the adjacent energy levels becomes slightly smaller. Therefore, transitions with the same Δv have a slightly different exciting frequency. The frequency shift causes a broadening in absorption bands. For example, the transitions of 1→2, 2→3 and 3→4 cause broadening around the fundamental vibration absorption. Therefore, the overtone-excited near-infrared region is of great interest.

1.2.3 Numerical simulation

In my work, I used two simulation software solutions: Lumerical FDTD and COMSOL multiphysics.

Lumerical FDTD is based on the Finite Difference Time Domain (FDTD) method which was developed in 1966 [34]. It solves Maxwell's equations without any physical approximation. In this method, the domain of the simulation is divided into a grid of points as shown in Fig. 6a. In the first step, the equations are solved for the initial time. Then, the

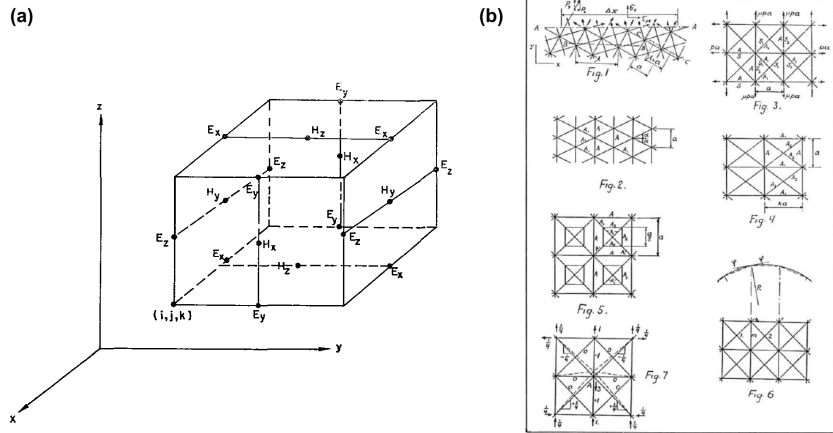


Figure 6: Schemes of the numerical simulation methods: (a) Yee scheme for finite difference time domain (FDTD) method [34] and (b) finite element method (FEM) scheme [35].

time progresses one step and the equations are solved again. This time-domain method can therefore be used for a range of frequencies in one simulation, as opposed to other methods.

COMSOL multiphysics is based on the Finite Element Method (FEM) which was first offered in 1941 [35]. This method is based on discretization for an approximation of the real solution to the partial differential equations. In this method, the domain of the simulation is divided into small elements (as shown in Fig. 6b) and solved for each element. The solutions are then connected for the solution of the whole domain. Due to the meshing method, FEM can be used for complicated structures and localized electromagnetic fields.

1.2.4 Experimental setup

My work included the construction of a homemade system to couple the light from a broadband laser source both inside and outside the waveguide to an optical spectrum analyzer, as shown in Fig. 7.

The first part of the system is the coupling of a broadband source inside an optical fiber as shown in Fig. 7a. The output of a broadband laser source (Fianium WL-SC-400-8-PP) was held by a v-groove that was placed on a 3D stage. The collecting pigtail optical fiber was placed on the second 3D stage. A 10x objective was placed in a fixed location on the second stage. The distance between the objective and the fiber connector was estimated as the objective working distance (10.6 mm). The output of the fiber was connected to the optical spectrum analyzer (OSA, Yokogawa AQ6370) with a resolution of 1 nm and a sampling interval of 0.2 nm. First, the laser was aimed at the center of the objective for an optimal starting calibration point. Due to the high power of the laser, an attenuator was placed after the laser to decrease the power and prevent high reflection, which harms the

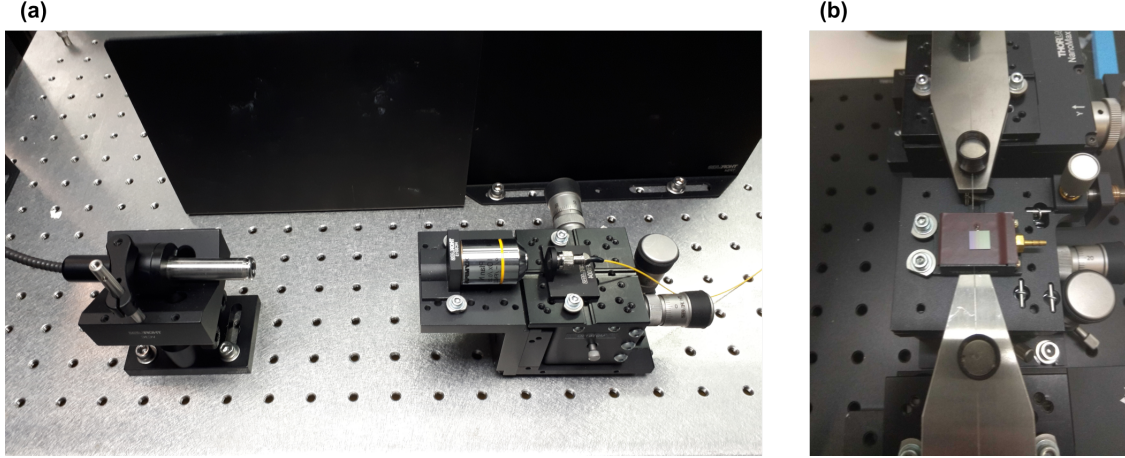


Figure 7: (a) The coupling setup of laser to fiber. (b) The waveguide input and output coupling setup.

alignment of the laser by causing dazzle. Next, the attenuator was removed and the fiber was aligned for a smooth and high power spectrum.

The second part of the system is: coupling the light inside the waveguide and collecting the waveguide output as shown in Fig. 7b. The problem is that the divergence angle of the fiber output is 0.13 rad (4.75 degrees), which creates a beam wider than the waveguide facet. This creates big coupling losses. Therefore, for coupling the laser into the waveguide I used a lensed fiber with a waist diameter of $4.2 \mu\text{m}$ and a working distance of $13 \mu\text{m}$. The single-mode fiber was connected to the lensed fiber using an FC/PC to FC/PC mating sleeve. The lensed fiber was held with a v-groove which was placed on a precise 3D stage. Another problem is that a small angle between the fibers and the waveguide can cause a problem with the coupling. Therefore, the waveguide was placed on a 3D stage with a rotation stage for verifying that the waveguide and fibers were aligned at the same angle. The waveguide output was collected with another pigtail fiber, held with a v-groove placed on a precise 3D stage. The output was collected to an optical spectrum analyzer. The whole waveguide coupling system was monitored by a microscope for precise alignment.

1.2.5 The fabrication process of microfibers

One of the methods I used to enhance sensitivity was by decreasing the confinement of the mode in guided wave structure. By minimizing the dimensions of the guiding medium, the confinement of the mode decreases. As a result, the fraction of the power and the penetration depth of the evanescent field increases. As a guided wave architecture I used a tapered fiber, as illustrated in Fig. 8a. To check the influence of decreasing the confinement of the mode on sensitivity, I fabricated a microfiber by tapering a commercial optical fiber,

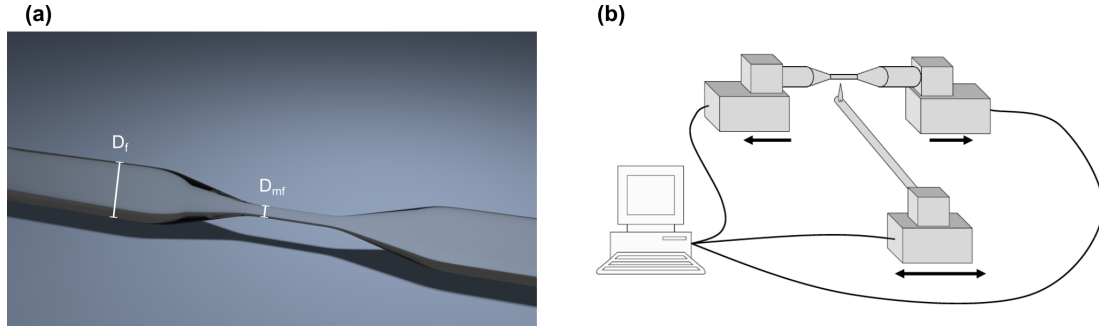


Figure 8: (a) Illustration of a tapered fiber. (b) Illustration of the tapering machine [36].

as illustrated in Fig. 8b. The single-mode fiber (SMF-28) was tapered to approximately $2.5 \mu\text{m}$ diameter, using a commercial Vytran GPX-3000 tapering system. In the first step, the acrylate polymer coating was removed from the tapering area. The tapering process was divided into two steps. First, the fiber was tapered from a diameter of $125 \mu\text{m}$ to a diameter of $\sim 15 \mu\text{m}$. Next, the fiber was tapered from a diameter of $\sim 15 \mu\text{m}$ to a diameter of $\sim 2.5 \mu\text{m}$. The tapered fiber was glued on both sides with epoxy glue to a metal fork, which I designed and fabricated for achieving durability in the fragile microfiber region. A Teflon spacer, to be used as a liquid reservoir due to its surface tension and hydrophobic attributes, was placed under the tapered fiber.

1.2.6 Focused Ion Beam (FIB) technique

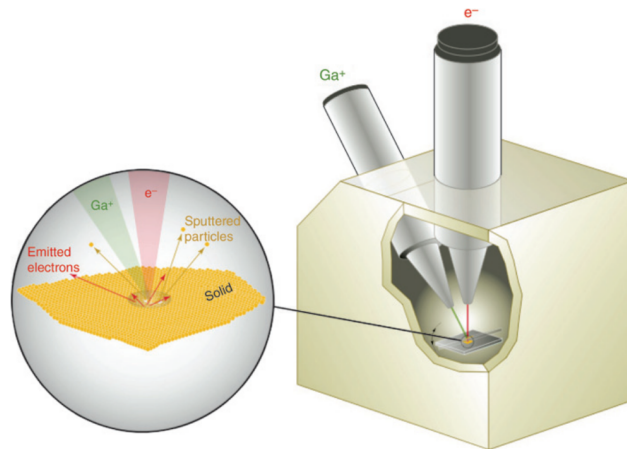


Figure 9: Illustration of a FIB-SEM dual-beam with a zoom of the electrons and ion beam interaction with the sample [37].

For fabrication of the structure in the waveguide, I used a Focused Ion Beam (FIB) technique, illustrated in Fig. 9. This technique was first used in field ion microscopes and

later adopted by the semiconductor industry. This method is similar to the scanning electron microscope (SEM) technique, but instead of a beam of electrons a beam of ions, usually gallium (Ga), is used. The beam hits the substrate, sputtering the material in a controllable manner. This technique allows the fabrication of structures at nanometer–micrometer scale and can be used for fabrication of small unit-cell structures, such as parallelepipedal dielectric metasurface for enhancing dipole moment [38] and anti-reflective metasurface [39]. The imaging in the FIB machine is made by detection of the electrons emitted in the interaction between the ions and the material, or by an additional SEM column. Furthermore, by using different gas-injection sources, the FIB machine can locally deposit conducting material (W, Pt, or C) or insulating material (SiO_2). As a result, the FIB machine can be used for depositing, sputtering and imaging, and is an important tool in the fabrication of micro- and nanoscale structures on a waveguide.

2 Published papers

2.1 Si Nanostrip Optical Waveguide for On-Chip Broadband Molecular Overtone Spectroscopy in Near-Infrared

The first step in my research was to study the vibrational overtone absorption on a multimode rib silicon waveguide [32].

The investigation of fundamental vibrations is performed in many systems. However, overtone transitions are overlooked due to their low absorption cross-section. I investigated the overtone absorption of aromatic amines, such as aniline and *N*-methylaniline (NMA), using Silicon-on-Insulator (SOI) multi-mode rib waveguides [32]. Primary and secondary amines are of tremendous importance because they are the major signal of environmental pollution and are also widely used in the dye and pharmaceutical industries [40]. I investigated optical waveguides, since one can tune the optical mode and the evanescent field interaction with the analyte to achieve superior sensitivities.

In this experiment, I used a silicon rib waveguide with a height of 2 μm , strip thickness of 400 nm and width of 16 μm . A supercontinuum generation laser source was coupled into a single-mode fiber and aligned using a piezoelectric translation stage into the waveguide. The output signal was collected via multi-mode fiber into an optical spectrum analyzer. 3 μl of *N*-methylaniline and Aniline were dropped on the waveguide separately and the output spectrum was measured. The absorption bands of *N*-methylaniline of the vibrational mode of the N-H first overtone and the C-H second overtone around 1.2 μm [41] were seen, in addition to the differences in the transmission of aniline and *N*-methylaniline with different concentrations. Moreover, changes in the absorption band of the first overtone of N-H in *N*-methylaniline and aniline were successfully detected around 1.5 μm . The N-H bond overtone absorption in aniline has a red shift and *N*-methylaniline a blue shift, around 1.5 μm . The absorption band of aniline is wider compared to that of *N*-methylaniline, due to the excitation of combination molecular vibrational modes [42].

From these results, I concluded that the sensitivity of the optical waveguide made of silicon can be increased by more than 3 orders of magnitude compared to the numerical simulation, due to the excitation of high-order guided modes. Due to the large evanescent field and increased interaction with the analyte, high-order modes contribute to the sensitivity of the sensor. In addition, proof is shown of the excitation of molecular vibrations overtones using a straight waveguide spectroscopy tool.

Si Nanostrip Optical Waveguide for On-Chip Broadband Molecular Overtone Spectroscopy in Near-Infrared

Aviad Katiyi¹ and Alina Karabchevsky*^{2,3}

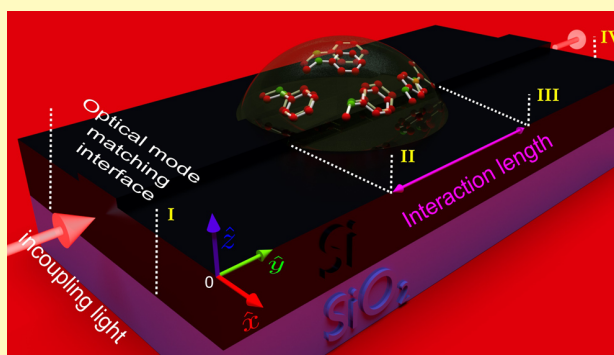
Electrooptical Engineering Unit, Ben-Gurion University of the Negev, David Ben Gurion Blvd, P.O. Box 653, Beer-Sheva 8410501, Israel

Ilse Katz Institute for Nanoscale Science & Technology, Ben-Gurion University of the Negev, David Ben Gurion Blvd, P.O. Box 653, Beer-Sheva 8410501, Israel

Center for Quantum Information Science and Technology, Ben-Gurion University of the Negev, David Ben Gurion Blvd, P.O. Box 653, Beer-Sheva 8410501, Israel

ABSTRACT: The ability to probe the molecular fundamental or overtone (high harmonics) vibrations is fundamental to modern healthcare monitoring techniques and sensing technologies since it provides information about the molecular structure. However, since the absorption cross section of molecular vibration overtones is much smaller compared to the absorption cross section of fundamental vibrations, their detection is challenging. Here, a silicon nanostrip rib waveguide structure is proposed for label-free on-chip overtone spectroscopy in near-infrared (NIR). Utilizing the large refractive index contrast ($\Delta n > 2$) between the silicon core of the waveguide and the silica substrate, a broadband NIR lightwave can be efficiently guided. We show that the sensitivity for chemical detection is increased by more than 3 orders of magnitude when compared to the evanescent-wave sensing predicted by the numerical model. This spectrometer distinguished several common organic liquids such as *N*-methylaniline and aniline precisely without any surface modification to the waveguide through the waveguide scanning over the absorption dips in the NIR transmission spectra. Planar NIR Si nanostrip waveguide is a compact sensor that can provide a platform for accurate chemical detection. Our NIR Si nanostrip rib waveguide device can enable the development of sensors for remote, on-site monitoring of chemicals.

KEYWORDS: molecular vibrations, overtones, near-infrared, waveguide, on-chip, nanosensor



Spectroscopy focuses on the interaction between light and matter. This interaction results in absorption or emission of radiation due to the change in molecular energy. The energy appears in different regions of the electromagnetic spectrum and gives distinctive information about the molecular structure therefore, infrared spectroscopy is certainly one of the most important analytical techniques available to today's scientists. In the mid-infrared (MIR) region of the electromagnetic spectrum, the fundamental vibrations can be excited, resulting in well pronounced absorption lines that mitigate the identification of molecular bonds. However, their high molecular absorption coefficient prevents large penetration depth and an adjustment of sample thickness. As opposed to the MIR, near-infrared (NIR) radiation excites overtone and combination vibrational modes and allows direct analysis of strongly absorbing and highly scattering samples without further pretreatments. Albeit, absorption cross section of molecular vibration overtones is much smaller compared to the fundamental vibrations and therefore molecular vibration overtones are challenging to detect.

Optical waveguides platform¹ operating in NIR region can be used for remote and on-site detection in applications such as monitoring urban pollutants, toxins, volatile industrial elements, and certain military threats. The major drawback of current sensors is the specificity requirement determined by the functionalization of the sensor's surface. This additional process of surface modification is aimed at identification of specific chemicals. For instance, refractometers are sensors, which rely on a change in refractive index,^{2–6} and therefore they lack in identification of unlabeled analytes and bioentities since the refractive index of many of them could be similar. In addition, many different biochemical species coexist in a biological sample and these species register nearly indistinguishable shifts of refractive index when adsorbed onto the sensors. This results in a difficulty of multichannel detection of group of analytes since different areas of such sensor have to be differently prepared or pretreated with different antibodies^{7–9} or markers.

Received: November 22, 2017

Accepted: February 13, 2018

Published: February 13, 2018

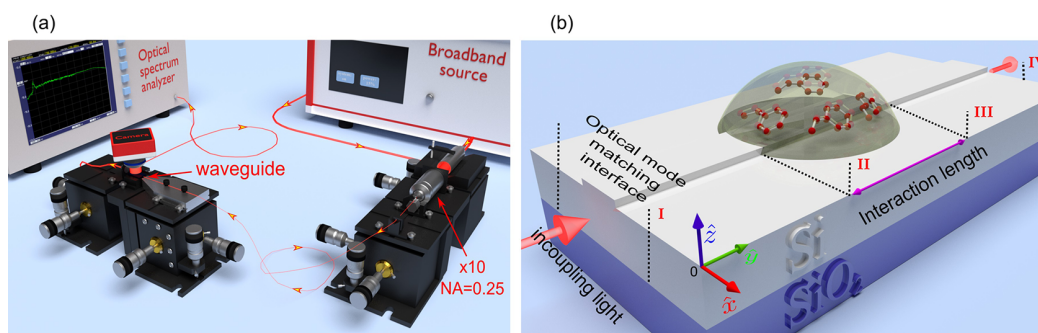


Figure 1. (a) Illustration of the experimental setup. Broadband NIR laser source is coupled to the single-mode fiber using a microscope objective. The fiber is butt-coupled to the input facet of the waveguide. The output signal is collected by the multimode fiber into the optical spectrum analyzer. The waveguides are imaged on the camera for the inspection, characterization and alignment. The propagation direction of light is indicated by the arrows. (b) Schematic of a Si nanostrip rib structure. Incident light illuminates the waveguide facet. The liquid is placed on the waveguide within the interaction length where the optical absorption for spectrum scanning takes place.

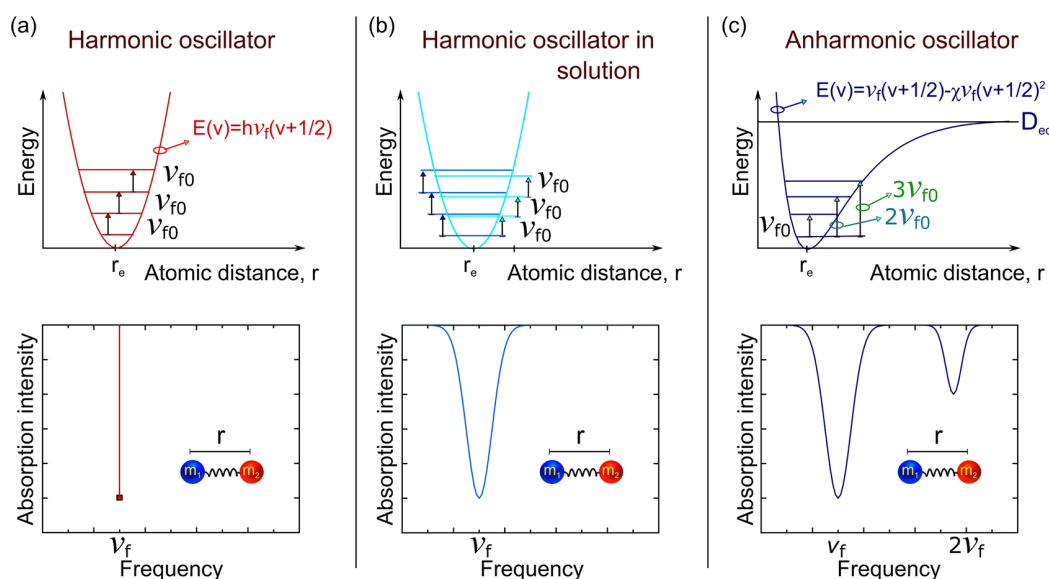


Figure 2. Diagrams of an oscillator mechanism described by the energy levels (top) and the corresponding spectral transmittance patterns (bottom) for (a) harmonic oscillator, (b) harmonic oscillator with the heterogeneity of the medium, and (c) anharmonic oscillator. Dissociation energy and the equilibrium bond distance are indicated by D_e and r_e , respectively.

Microresonator based sensing architectures,^{10–13} in contrast, demonstrate high sensitivity at a specific wavelength. However, due to the inherent property of the narrow free spectral range (FSR), these devices cannot provide broadband sensing.¹⁴ Mid-infrared spectroscopy is an efficient detection method which allows for label-free sensing.^{15–17} In contrast to the sensing techniques mentioned above, mid-infrared radiation is absorbed by molecular bonds, resulting in well-defined fundamental vibrations represented by absorption bands in the spectrum.¹⁸ Common equipment such as Fourier transform infrared (FTIR) spectrometers^{19,20} or wavelength scanning monochromators show mid-infrared spectra but they are bulky and much larger than a chip-scale sensor. Chip-scale mid-infrared sensors were reported^{21,22} for detection of common chemicals such as *N*-bromohexane, toluene, and isopropanol. Near-infrared spectrophotometers are widely used for acquiring near-infrared spectra using a cuvette as a liquid reservoir. Similar to the FTIR spectrometer, near-infrared spectrophotometers use benchtop equipment that is too large for monolithic integration on a chip. Chalcogenide waveguides²³ were proposed to probe molecular

overtone in near-infrared while integrated with microfluidic chip. Glass-based waveguides showed well-defined amine overtone absorption band around 1.5 μm in the diffusive regime.²⁴ However, these waveguides were pretreated by negative charge using plasma oxygen which is not suitable for on-site long-time measurements.

Here, we present a new chip-scale photonic device that utilizes NIR absorption by molecular vibration overtones for label-free chemical sensing. We designed a multimode silicon nanostrip waveguide in such a way, that launching the high order modes improves the sensitivity of the chip-scale device for broadband detection. Reducing the height of the nanostrip will prevent the excitation of high order modes and affect the sensitivity. We experimentally demonstrate that this NIR on-chip sensor can distinguish between different organic liquids. Our NIR Si nanostrip rib waveguide device can enable the development of sensors for remote, on-site monitoring of chemicals and more.

RESULTS AND DISCUSSION

Figure 1a shows an illustration of our experimental setup for the demonstration of the effect. The broadband laser source (Fianium WL-SC-400-15) was coupled to a single-mode fiber. The fiber was held with a piezoelectric stage which allows for precise adjustment of the fiber to the waveguide. The output signal was collected via multimode fiber into an optical spectrum analyzer (Yokogawa AQ6370D). The waveguide surface was imaged onto a camera of the inverted microscope for the accurate inspection.

The proposed sensor shown in Figure 1b has dimensions of 5 mm (L) × 5 mm (W) × 1 mm (D) and supports nine guided modes. Due to the large evanescent field and increased interaction with the analyte, high order modes contribute to the sensitivity of the sensor. We found that, in Si nanostrip configuration, the sensitivity of the sensor does not change beyond nine modes. The effect of enhanced NIR absorption was realized in butt-coupled experiments. To demonstrate the effect, the sensor was butt-coupled to the single-mode fiber and illuminated by the broadband source. The broadband source allows for identifying multiple absorption bands and enables identification of multiple bonds in the analyte. Although sophisticated on-chip spectrometers have been demonstrated in MIR²¹ and NIR,^{1,14,23,24} broadband NIR spectrometers have never been shown for detection of molecular vibration overtones for spectral tracing with Si nanostrip.

It is known that the NIR spectroscopy is based on molecular overtones and combination modes vibrations with transitions which are forbidden by the selection rules of quantum mechanics.²⁵ Transition probability $R_{i,j}$ describes the possibility of transition from lower i to higher j energy level defined by

$$R_{i,j} \propto \int \psi_i M \psi_j d \quad (1)$$

with wave function ψ and transition moment operator M . Due to the selection rule, only transition of $\Delta v = \pm 1$ is allowed in the harmonic oscillator model. The energy differences between the adjacent energy levels are constant, resulting in the absorption of only a photon with the exact energy that fits the frequency of the oscillator, ν_0 , as shown in Figure 2a. The frequency that leads to the transition from $v = 0$ to $v = 1$ is the fundamental frequency.

Ideally, in the harmonic model, the absorption spectra occur at a discrete frequency with zero width (Figure 2a). However, in practice, the absorption has nonzero width along the spectrum (Figure 2b). This occurs because the harmonic model describes a single diatomic molecule or identical diatomic molecules. In practice, the diatomic molecules are not identical because they are embedded in a heterogeneous solution. For this reason, a molecule is influenced slightly differently by the surroundings. As a result, the vibration frequency for the same transition, for example the fundamental frequency, is a little shifted in different molecules, resulting in broadening of the absorption as shown in Figure 2b. Anharmonic models influence the spectra in few ways. First, the energy differences between the adjacent energy levels are slightly different. This results in a group of absorptions of the same Δv (for example: $0 \rightarrow 1$, $1 \rightarrow 2$, and $2 \rightarrow 3$), which results in broadening of the spectral line. Second, the transition rule of the harmonic model is not applied in the anharmonic model, which allows vibration transitions of $\Delta v \neq 1$. Few absorption bands will appear in the spectrum, as shown in Figure 2c. The frequencies that result in those transitions are called overtones or higher harmonics and

they are the topic of this paper. Due to the lower probability of the overtone transitions, the first overtone is smaller by a factor of 10 compared to the fundamental transition.²⁶ The probability of higher order overtones transitions also decreases as factor 10, therefore, detection of molecular overtones is challenging.²⁶ As mentioned above, the great advantage of the NIR spectroscopy is the large penetration depth into the analyte. Therefore, broadband NIR spectroscopy can be very useful in probing bulk material without special sample preparation, surface functionalization or surface treatment.

In this paper, we describe NIR transparent chip-based device that utilizes an optical nanostrip rib waveguide to guide a broadband light for efficient monitoring of analytes. We suggest a new approach that can allow the NIR light to interact with bulk analyte and efficiently excite molecular vibration overtones. This device provides improvements over current evanescent-wave detection using diffused waveguides,²⁴ ring resonators,¹⁴ or channel waveguides^{1,23} in three ways: (1) the availability in detection over a broad spectral range (from $\lambda = 1.1 \mu\text{m}$ to $\lambda = 1.65 \mu\text{m}$), (2) efficient coupling to high order modes significantly enhances the interaction between the evanescent field and the analyte and imparts high sensitivity to this device, and (3) no need of surface treatment.

In Figure 1a, we illustrate the structure of the NIR silicon nanostrip sensor device. The sensing element is a nanostrip rib waveguide with two end-facets butt-coupled to optical fibers. The optical fiber is launched into the nanostrip rib waveguide. The hydrophobicity of the device due to the 2 nm thick layer of the native oxide on Si, confines the liquids within the interaction length. Thus, the Si nanostrip rib structure serves as (a) an efficient NIR medium for transmitting the NIR light and (b) fluid confining element. After passing through the interaction length, the NIR probe light contains the fingerprint of the analyte as an absorption bands. It is subsequently recorded by a vis/near-IR optical spectrum analyzer. The transmitted light contains the absorption spectrum of the analyte. Each absorption band is related to different atomic bonds in the analyte.

To illustrate the layout of the NIR nanostrip rib waveguides and their corresponding NIR response, we highlight four interfaces (Figure 1a): (I) the infacet where the in-coupling light from the optical fiber couples to the waveguide, (II) and (III) the interfaces between the waveguide and the analyte, and (IV) the endfacet where the out-coupling light from the waveguide couples to the optical fiber. The waveguide guiding layer is made of silicon and the substrate is made of silica. The sensing area is located within the interaction length and between interface II and III. The guidance is provided by total internal reflection at the interfaces with air and the SiO₂ substrate. The total broadband optical transmittance of the device is defined primarily by the losses of the power within the interaction length and therefore is obtained as in ref 27:

$$T = \left| \sum_{\gamma_1=0,1,\dots,8} C_{\gamma_1} \exp(-\alpha_{\gamma_1} L) \right|^2 \quad (2)$$

where $C_{\gamma_1} = (I_{\gamma_0,\gamma_1} + I_{\gamma_1,\gamma_0})^2 / (4I_{\gamma_0,\gamma_0}I_{\gamma_1,\gamma_1})$ and L is the interaction length. α is an attenuation coefficient in dB/cm of modes²⁷ in a region filled with the analyte $0 < y < L$, and $\gamma_0 = 0, 1, \dots, 8$ are the guided modes in regions I, II and $\gamma_1 = 0, 1, \dots, 8$ are the guided modes in regions II, III influenced by the analyte.

Figure 3 shows scanning electron microscopy (SEM) images of the fabricated Si nanostrip rib waveguides. A clearly resolved

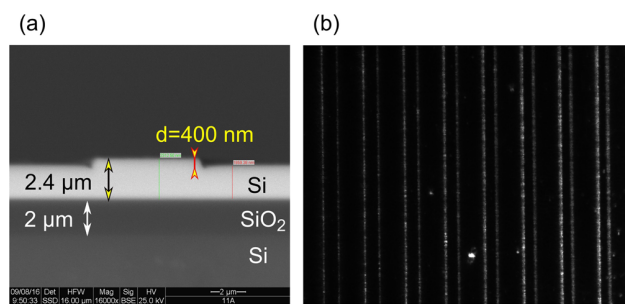


Figure 3. Images of the Si nanostrip waveguide. (a) SEM image of the waveguide cross section. (b) Top view of the rib waveguide showing the scattering effect of waveguide walls.

400 nm thick nanostrip is etched on the Si forming the Si layer of 2.4 μm . Then 2 μm silica layer is sandwiched between the guiding layer and the silicon substrate to fulfill the guidance condition. Figure 3b shows a top view of the rib waveguides of different widths of the strip. The scattered light is due to the roughness of the waveguide walls.

The chemical sensitivity of our rib nanostrip waveguide²⁸ was simulated using finite-difference time-domain (FDTD) and finite-element method (FEM) numerical solvers. We determined sensitivity by calculating the fraction of the evanescent field:

$$\eta_{\text{evanes}} = \frac{P_{\text{analyte}}}{P_{\text{total}}} = \frac{\iint_{\text{analyte}} S \, dA}{\iint_{-\infty}^{\infty} S \, dA} \quad (3)$$

With time varying Poynting vector S defined as

$$S = \frac{1}{2} \Re\{EH^*\} \quad (4)$$

The absorption is caused due to the excitation of molecular vibration overtone, mathematically described by the complex refractive index of the liquid; therefore, the electric E and magnetic H fields in a waveguide evolve as complex.

Using FDTD solver, we studied the modes and their absorption for rib waveguide at wavelength of 1.5 μm . Higher order modes have greater absorption here, due to the strong evanescent field. Figure 4a and b shows the predicted optical field profiles (TE and TM, respectively) for propagating NIR radiation, wavelength of $\lambda = 1.5 \mu\text{m}$ within a rib waveguide with pure *N*-methylaniline as analyte. Figure 4c and d shows the absorption of TE modes and TM modes, respectively.

Figure 4a and b shows that in the silicon rib waveguide the fundamental mode is highly confined at the center of the waveguide core and interacts weakly with the analyte for both TE and TM modes. In addition, it is shown in Figure 4c and d that the absorbance for a low order modes in the silicon rib waveguide have very low absorption. Thus, exciting higher order modes will contribute to the enhancement of the evanescent field, which consequently improves the sensitivity of the sensor.¹

It is important to understand the evolution of the modes due to the abrupt discontinuity in the medium in which the nanostrip is embedded. Specifically, the abrupt change in the medium affects the guided modes, resulting in a unique spectral

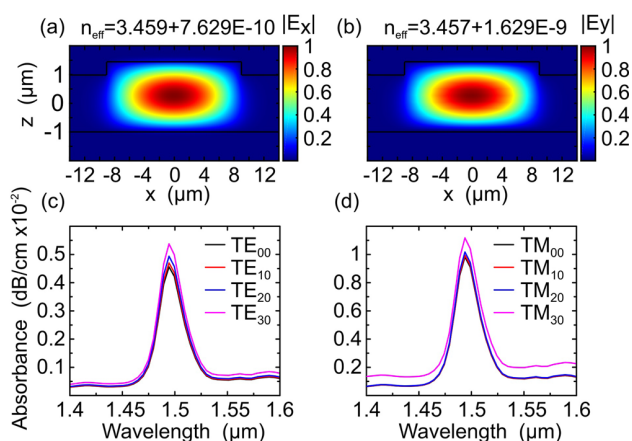


Figure 4. Calculated normalized fundamental mode intensity profile of a Si nanostrip rib waveguide at $\lambda = 1.5 \mu\text{m}$ of (a) fundamental TE and (b) fundamental TM. (c) Absorbance of $\text{TE}_{\gamma 1, n}$ modes. (d) Absorbance of $\text{TM}_{\gamma 1, n}$ modes. Note: For here $\gamma 1 = 0, 1, 2, 3$ for simplicity of visualization. However, the calculations were performed for all nine $\gamma 1 = 0, 1, \dots, 8$ modes.

signature of the molecule under investigation. Figure 5 shows the cross section color maps of the evolution of normalized

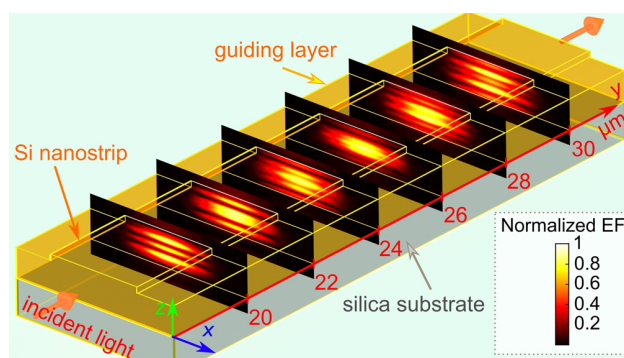


Figure 5. Evolution of the interfered guided modes in the interaction length with the analyte. Calculated normalized mode profiles using FDTD, with different distance d from the beginning of the interaction region at the point of $y = \text{II}$. d is indicated on each subplot. The amplitude of normalized electric field (EF) is presented in the inset.

mode profiles exhibiting interference and guided in the interaction length of the designed waveguide (Figure 1a). A Gaussian beam, wavelength of 1.5 μm , radius of 4.75 μm , and divergence angle of 0.13 rad, was launched into the waveguide. The analyte was explored at a distance d of $y = 10 \mu\text{m}$ from the waveguide infacet at the point of $y = \text{I}$. In the simulation $y(\text{I}) = 0$, the cross sections of the calculated normalized mode profiles were performed at distances of $y = 20, 22, \dots, 30 \mu\text{m}$ with an interval of 2 μm from the beginning of the interaction length at the point of $y = \text{II}$ as shown in Figure 5.

For the validation of the proposed structure as efficient near-infrared sensor, we explored *N*-methylaniline, aniline, and mixture of *N*-methylaniline in hexane. These analytes have absorption bands of the first overtone of the amine group N–H around 1.5 μm .²⁹ During the experiment, the analyte with volume of 3 μL was dripped into the waveguide surface defining the interaction length of 2 mm. Figure 6 shows the

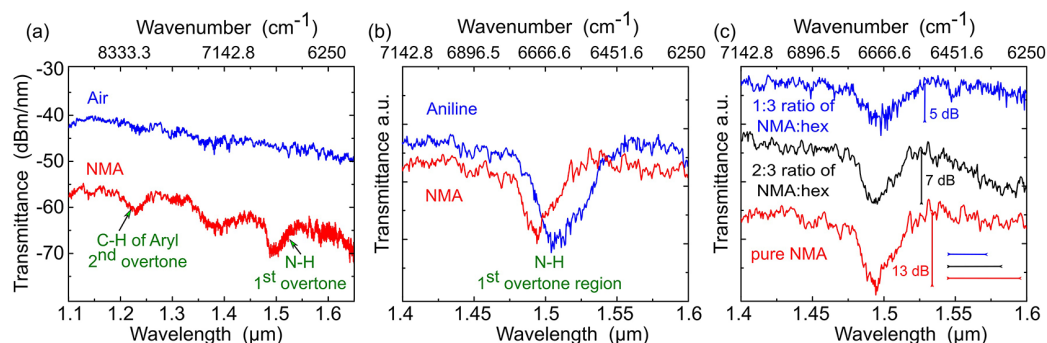


Figure 6. Spectral characterizations using on-chip Si nanostrip rib waveguide NIR spectrometer. (a) Transmittance spectra of pure *N*-methylaniline (NMA). As a reference, we measured the transmittance through the waveguide in air. (b) Transmittance spectra of *N*-methylaniline and aniline. (c) Transmittance spectra of pure *N*-methylaniline molecule and mixture ratios of 1:3 and 2:3 of *N*-methylaniline in hexane, NMA/hex, with indicated absorption depths of the analytes. In addition, the bars are placed next to each other for clear comparison of absorption depths.

experimental results performed on silicon nanostrip rib waveguide experiments.

Figure 6a shows absorption bands of *N*-methylaniline around 1.5 and 1.2 μm which correspond to the molecule vibrational modes of first N–H overtone and second C–H overtone,³⁰ respectively. Figure 6b clearly shows differences in the transmission of *N*-methylaniline and aniline. The absorption bands of first overtone of N–H in *N*-methylaniline and aniline was successfully detected around 1.5 μm. The absorption band of aniline is wider compared to the absorption band of *N*-methylaniline. The broadening of aniline absorption on the N–H first overtone can be explained by the excitation of combination molecular vibrational modes.^{29,31} Figure 6c shows the transmission spectra of the pure *N*-methylaniline molecule and mixture ratios 1:3 and 2:3 of NMA/hexane. It demonstrates the ability to detect and study the absorption of different mixtures ratio of NMA/hexane using a silicon rib waveguide. The waveguide is illuminated by the optical fiber with angular divergence, and therefore with other modes (orthogonal to each other) coexisting. Each optical mode has a discrete propagation constant β . The coupling efficiencies (from fiber to waveguides) including the insertion and propagation losses were -30 dB. Even with obtaining such a high loss, the molecular signature overtones were detected on the devices reported here.

CONCLUSIONS

In conclusion, we proposed a silicon nanostrip rib waveguide structure for label-free on-chip overtone spectroscopy in NIR. We show that, utilizing the large refractive index contrast ($\Delta n > 2$) between the Si core of the waveguide and the SiO₂ substrate, a broadband NIR lightwave can be efficiently guided. In addition, we show that the sensitivity for chemical detection is increased by more than 3 orders of magnitude when compared to the evanescent-wave sensing predicted by the numerical model. Our on-chip spectrometer distinguished several common organic liquids such as *N*-methylaniline and aniline precisely without any guide's surface modification through the spectral scanning over the absorption dips in the NIR transmission spectra. Planar NIR silicon nanostrip waveguide is a compact sensor which can provide a platform for accurate chemical detection. Our NIR silicon nanostrip rib waveguide device can enable the development of sensors for remote, on-site monitoring of chemicals.

MATERIALS AND METHODS

Chemicals. Aniline (C₆H₅NH₂, $\geq 99.5\%$), hexane (C₆H₁₄, $\geq 95\%$), and *N*-methylaniline (C₆H₅NH(CH₃), $\geq 98\%$) were purchased from Sigma-Aldrich.

Fabrication. Silicon layer was e-beam evaporated on silicon wafer. The rib patterns were first created with conventional photolithography and then etched.

Waveguide Characterization. We measured the waveguide dimension using a Stylus Profilometer, Veeco Dektak-8.

Simulation. The three-dimensional simulation was performed using a commercial Maxwell solver: Lumerical FDTD (Finite Difference Time Domain) solutions.

Spectroscopy on a Waveguide. The broadband laser source (Fianium WL-SC-400-15), bandwidth from 450 to 2400 nm, was focused into the single mode fiber (1550BHP) using an X10 plan achromat objective (Olympus) with a numerical aperture of NA = 0.25. The fiber was aligned with the waveguide using a stereo microscope (Zeiss Stemi SV6). The spectra were collected using the multimode fiber into the optical spectrum analyzer (Yokogawa 6370D).

AUTHOR INFORMATION

Corresponding Author

*E-mail: alinak@bgu.ac.il.

ORCID

Aviad Katiyi: 0000-0002-7924-9065

Alina Karabchevsky: 0000-0002-4338-349X

Notes

The authors declare no competing financial interest.

ACKNOWLEDGMENTS

The authors acknowledge the support of the Multidisciplinary Program Health-Engineering Sciences grant by the Ben-Gurion University of the Negev. The authors thank Dr. Avi Niv for kindly lending the supercontinuum light source to perform the measurements. The authors also acknowledge the help of Benyimin Hadad in obtaining the SEM images.

REFERENCES

- Katiyi, A.; Karabchevsky, A. Figure of merit of all-dielectric waveguide structures for absorption overtone spectroscopy. *J. Lightwave Technol.* **2017**, *35*, 2902–2908.
- Karabchevsky, A.; Tsapovsky, L.; Marks, R. S.; Abdulhalim, I. Study of immobilization procedure on silver nanolayers and detection of estrone with diverged beam surface plasmon resonance (SPR) imaging. *Biosensors* **2013**, *3*, 157–170.

- (3) Karabchevsky, A.; Karabchevsky, S.; Abdulhalim, I. Nano-precision algorithm for surface plasmon resonance determination from images with low contrast for improved sensor resolution. *J. Nanophotonics* **2011**, *5*, 051813.
- (4) Karabchevsky, A.; Karabchevsky, S.; Abdulhalim, I. Fast surface plasmon resonance imaging sensor using Radon transform. *Sens. Actuators, B* **2011**, *155*, 361–365.
- (5) Wang, Q.; Farrell, G. All-fiber multimode-interference-based refractometer sensor: proposal and design. *Opt. Lett.* **2006**, *31*, 317–319.
- (6) Schroeder, K.; Ecke, W.; Mueller, R.; Willsch, R.; Andreev, A. A fibre Bragg grating refractometer. *Meas. Sci. Technol.* **2001**, *12*, 757.
- (7) Shia, W. W.; Bailey, R. C. Single domain antibodies for the detection of ricin using silicon photonic microring resonator arrays. *Anal. Chem.* **2013**, *85*, 805–810.
- (8) Kurihara, Y.; Takama, M.; Sekiya, T.; Yoshihara, Y.; Ooya, T.; Takeuchi, T. Fabrication of carboxylated silicon nitride sensor chips for detection of antigen-antibody reaction using microfluidic reflectometric interference spectroscopy. *Langmuir* **2012**, *28*, 13609–13615.
- (9) Tromberg, B. J.; Sepaniak, M. J.; Alarie, J. P.; Tuan, V. D.; Santella, R. M. Development of antibody-based fiber-optic sensors for detection of a benzo [a] pyrene metabolite. *Anal. Chem.* **1988**, *60*, 1901–1908.
- (10) Wan, J.; Johnson, M. L.; Guntupalli, R.; Petrenko, V. A.; Chin, B. A. Detection of Bacillus anthracis spores in liquid using phage-based magnetoelastic micro-resonators. *Sens. Actuators, B* **2007**, *127*, 559–566.
- (11) Ksendzov, A.; Lin, Y. Integrated optics ring-resonator sensors for protein detection. *Opt. Lett.* **2005**, *30*, 3344–3346.
- (12) Sumetsky, M.; Windeler, R.; Dulashko, Y.; Fan, X. Optical liquid ring resonator sensor. *Opt. Express* **2007**, *15*, 14376–14381.
- (13) Li, M.; Wu, X.; Liu, L.; Fan, X.; Xu, L. Self-referencing optofluidic ring resonator sensor for highly sensitive biomolecular detection. *Anal. Chem.* **2013**, *85*, 9328–9332.
- (14) Nitkowski, A.; Chen, L.; Lipson, M. Cavity-enhanced on-chip absorption spectroscopy using microring resonators. *Opt. Express* **2008**, *16*, 11930–11936.
- (15) Jin, T.; Li, L.; Zhang, B.; Lin, H.-Y. G.; Wang, H.; Lin, P. T. Real-Time and Label-Free Chemical Sensor-on-a-chip using Monolithic Si-on-BaTiO₃ Mid-Infrared waveguides. *Sci. Rep.* **2017**, *7*, 1–8.
- (16) Lin, P. T.; Giammarco, J.; Borodinov, N.; Savchak, M.; Singh, V.; Kimerling, L. C.; Tan, D. T.; Richardson, K. A.; Luzinov, I.; Agarwal, A. Label-Free Water Sensors Using Hybrid Polymer-Dielectric Mid-Infrared Optical Waveguides. *ACS Appl. Mater. Interfaces* **2015**, *7*, 11189–11194.
- (17) Wang, X.; Antoszewski, J.; Putrino, G.; Lei, W.; Faraone, L.; Mizaikoff, B. Mercury-cadmium-telluride waveguides—a novel strategy for on-chip mid-infrared sensors. *Anal. Chem.* **2013**, *85*, 10648–10652.
- (18) Vajda, V.; Pucetaite, M.; McLoughlin, S.; Engdahl, A.; Heimdal, J.; Uvdal, P. Molecular signatures of fossil leaves provide unexpected new evidence for extinct plant relationships. *Nature ecology & evolution* **2017**, *1*, 1093–1099.
- (19) Bhargava, R.; Levin, I. W. Fourier transform infrared imaging: theory and practice. *Anal. Chem.* **2001**, *73*, S157–S167.
- (20) Griffiths, P. R.; De Haseth, J. A. *Fourier transform infrared spectrometry*; John Wiley & Sons, 2007; Vol. 171.
- (21) Lin, P. T.; Kwok, S. W.; Lin, H.-Y. G.; Singh, V.; Kimerling, L. C.; Whitesides, G. M.; Agarwal, A. Mid-infrared spectrometer using opto-nanofluidic slot-waveguide for label-free on-chip chemical sensing. *Nano Lett.* **2014**, *14*, 231–238.
- (22) Yu, C.; Ganjoo, A.; Jain, H.; Pantano, C.; Irudayaraj, J. Mid-IR biosensor: detection and fingerprinting of pathogens on gold island functionalized chalcogenide films. *Anal. Chem.* **2006**, *78*, 2500–2506.
- (23) Hu, J.; Tarasov, V.; Agarwal, A.; Kimerling, L.; Carlie, N.; Petit, L.; Richardson, K. Fabrication and testing of planar chalcogenide waveguide integrated microfluidic sensor. *Opt. Express* **2007**, *15*, 2307–2314.
- (24) Karabchevsky, A.; Kavokin, A. Giant absorption of light by molecular vibrations on a chip. *Sci. Rep.* **2016**, *6*, 1–7.
- (25) Atkins, P. W.; Friedman, R. S. *Molecular quantum mechanics*; Oxford University Press, 2011.
- (26) Suart, B. *Infrared Spectroscopy: Fundamental and Applications*; John Wiley & Sons, Ltd, 2004.
- (27) Karabchevsky, A.; Wilkinson, J. S.; Zervas, M. N. Transmittance and surface intensity in 3D composite plasmonic waveguides. *Opt. Express* **2015**, *23*, 14407–14423.
- (28) Okamoto, K. *Fundamentals of optical waveguides*; Academic Press, 2010.
- (29) Whetsel, K. B.; Roberson, W. E.; Krell, M. Near-infrared spectra of primary aromatic amines. *Anal. Chem.* **1958**, *30*, 1598–1604.
- (30) Shaji, S.; Eappen, S. M.; Rasheed, T.; Nair, K. NIR vibrational overtone spectra of N-methylaniline, N, N-dimethylaniline and N, N-diethylaniline—a conformational structural analysis using local mode model. *Spectrochim. Acta, Part A* **2004**, *60*, 351–355.
- (31) Shaji, S.; Rasheed, T. Vibrational overtone spectra of chloroanilines—evidence for intramolecular hydrogen bonding in o-chloroaniline. *Spectrochim. Acta, Part A* **2001**, *57*, 337–347.

2.2 Deflected Talbot-Mediated Overtone Spectroscopy in Near-Infrared as a Label-Free Sensor on a Chip

The second step in my research was to investigate a new method to enhance sensitivity by coupling the power to a high order mode. I studied the influence of a cluster of inclusions on the sensitivity of an SOI rib waveguide by scattering [43].

Multi-mode interference (MMI) is a growing interest in integrated optics and can be used for a variety of applications such as couplers [44] and sensors [45]. The phenomena of a periodic structure that creates self-imaging were discovered in 1836 by Henry Fox Talbot [46] and named the Talbot effect. When a guided wave is transmitted through a multi-mode optical waveguide, it creates wavefront replicates of periodic perturbation patterns along the propagation direction of the guided wave, due to a multi-mode interference effect.

I investigated the influence of cylindrical inclusions through the guiding layer on the Talbot effect with multi-mode silicon rib waveguides. I explored numerically the Talbot effect on a multi-mode waveguide. When the cylindrical inclusions are milled in the waveguide, I notice an interesting field distribution pattern. It appears that the self-imaging effect is deflected due to the inclusions. To prove this effect, I studied a silicon nanostrip rib waveguide on silica - SiO_2 substrate with a height of $1.6 \mu\text{m}$ and nanostrip height of 400 nm with cylindrical inclusions in the guiding layer. I dripped a molecule with a volume of $3 \mu\text{l}$ of *N*-methylaniline on the waveguide. The output signal was collected by the multi-mode fiber into an optical spectrum analyzer. I found that the spectral signature of the molecular vibration overtones around $1.5 \mu\text{m}$ is clearly seen in the waveguide with the inclusions. However, when the waveguide is not perforated, evidence that the molecules are present on the waveguide surface is cloaked.

From these results, I concluded that the perturbation along the propagation direction of the guided mode embedded in the molecular medium enhances the absorption of the molecular transition overtones by transferring power to higher-order modes.

Deflected Talbot-Mediated Overtone Spectroscopy in Near-Infrared as a Label-Free Sensor on a Chip

Aviad Katiyi and Alina Karabchevsky*

Cite This: *ACS Sens.* 2020, 5, 1683–1688

Read Online

ACCESS |



Metrics & More



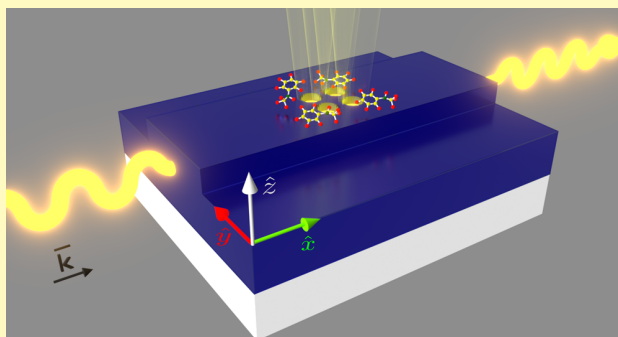
Article Recommendations



Supporting Information

ABSTRACT: Rapid, sensitive, and reliable detection of aromatic amines, toxic manufacturing byproducts, has been previously achieved with molecular vibrations in the mid-infrared (Mid-IR) region. However, Mid-IR spectroscopic tools are hampered by a need to prepare the samples and the sensor cost. Here, we develop an affordable label-free sensor on a chip, operating in near-infrared (NIR) for ultrasensitive detection of absorption line signatures based on molecular vibrations overtones of the aromatic amine *N*-methylaniline probe molecule. We design a perforated silicon rib waveguide and fabricate it by milling cylindrical inclusions through the waveguide core. The molecular signatures were monitored when waveguides are embedded in toxic *N*-methylaniline, experiencing a deflected Talbot effect. We observed that when the Talbot effect is deflected, the absorption lines in NIR are enhanced despite the weakly absorbing nature of the probe molecules. This new spectroscopic strategy can potentially be extended to detect other common toxic byproducts in a chip-scale label-free manner and to enhance the functionality of chemical monitoring.

KEYWORDS: molecular overtones, optical waveguide, multimode interference, near-infrared spectroscopy, integrated photonics



Multimode interference (MMI) devices have attracted growing interest in integrated optics^{1,2} widely used for a variety of applications such as communication,^{3,4} optical spectroscopy,⁵ and integrated photonics.^{6,7} MMI devices have a characteristic Talbot pattern. This pattern was discovered in 1836 by Talbot⁸ in a periodic structure such as diffraction grating, which creates a self-imaging effect. By illuminating a diffraction grating, Talbot observed repetition of color bands. Later, in 1881, this effect was rediscovered and explained by Rayleigh.⁹ When light passes through the periodic diffraction grating, it creates an image of the grating at distance z_T , which is named the Talbot length. The Talbot effect also occurs in multimode (MM) waveguides.^{10–12} However, in the MM waveguides, the Talbot effect is related to the different propagation constants of the guided modes but not to the periodicity of the input source. When a guided wave is transmitted through a multimode optical waveguide, it creates wavefront replicates of a periodic perturbation pattern along the propagation direction of the guided wave.¹³ This occurs due to the multimode interference effect. The MMI effect is used to minimize and improve the optical devices, such as Mach–Zehnder switches^{14,15} and modulators,¹⁶ and to enhance the functionality of integrated photonic circuits.

Our sensor is based on the MMI effect. It is important to note that MMI-based devices such as optical couplers have low propagation losses and allow for small device dimensions,¹³ which make them ideal for Mach–Zehnder interferometers¹⁷

and other integrated photonic components. In addition, the multimode interference effect in a waveguide can be used for sensing applications.¹⁸ A sensor based on MMI can achieve a resolution of 5.41×10^{-5} RIU.¹⁹ Instead of using the MMI effect on a slab waveguide, the MMI structure can be also created out of slot waveguides. Due to the changes in the refractive index inside the slot, the output then is changed, leading to the resolution of 9.8×10^{-5} RIU.²⁰ However, those structures behave as refractometers, which essentially lack in specificity. In contrary, spectrometers operating in low energies in infrared are specific since they are able to identify a molecular structure from the unique absorption lines.²¹ Despite the fundamental interest to understand the mechanism of absorption by molecular vibrations overtones, the probability of the overtone transition of $\Delta\nu > 1$ (ν is the number of the energy level) is very small. The overtone absorption is an order of magnitude smaller compared to the fundamental vibration absorption,²² which makes the detection of the overtone absorption challenging.^{23–25}

Received: February 19, 2020

Accepted: May 8, 2020

Published: May 8, 2020



Here, we study the deflected Talbot effect realized in a weakly absorbing molecular medium. To understand the mechanism underlying the deflected Talbot effect in a weakly absorbing medium, we combined several disciplines, namely, the physics of guided wave optics, the waveguide with inclusions fabrication routines, the surface chemistry, and the molecular overtone spectroscopy. We explore the overtone absorption by multimode interference (MMI) in multimode silicon rib waveguides and reveal that the deflected Talbot effect increases the probability of overtone transitions. Next, we investigate the influence of cylindrical inclusions in the guiding layer on the Talbot effect.

EXPERIMENTAL SECTION

Numerical Simulation. We built the three-dimensional (3D) model and performed simulations using a commercial Maxwell solver: Lumerical FDTD (finite difference time domain) solutions. A Gaussian beam, with a wavelength of 1.5 μm , radius of 4.75 μm , and divergence angle of 0.13 rad, was launched into a silicon-on-insulator (SOI) rib waveguide with a slab height of 1.6 μm , strip height of 0.4 μm , width of 8 μm , and waveguide length of 30 μm . The refractive indices of silicon and silica are $n_{\text{Si}}(1.5 \mu\text{m}) = 3.48$ and $n_{\text{SiO}_2}(1.5 \mu\text{m}) = 1.444$, respectively. The waveguide was embedded in *N*-methyl aniline ($n_{\text{NMA}}(1.5 \mu\text{m}) = 1.5712 + i8.931 \times 10^{-5}$)¹⁸ in a distance of 10 μm from the input facet. The cross section of the electric field in x - y and x - z planes was taken in the middle of the waveguide, $y = 0$ and $z = 1 \mu\text{m}$, respectively.

Waveguide Fabrication. The rib waveguide was fabricated on silicon-on-insulator (SOI) wafer (Si carrier, 2 μm SiO₂ and 2 μm Si). For the fabrication process, we used e-beam resist poly-methyl metacrylate (PMMA) 950K for writing the waveguides. After writing and developing the resist, we evaporated a hard mask of aluminum with a thickness of 50 nm via an electron gun evaporator. Next, we soaked the sample in acetone for 4 h as the lift-off process, and we cleaned the sample with isopropanol (IPA). Eventually, we dry-etched the sample with SF₆ + Ar and O₂, which enables us to get a straight line and 90° waveguide wall. We removed the residue of the Al using a 400K developer.

Inclusion Cluster Fabrication. The inclusions of cylindrical shape were milled into the silicon guiding layer using a Helios focused ion beam (FIB). The holes were fabricated with a depth of 2 μm and radius of 0.58 μm .

Spectroscopy on a Waveguide. A broadband laser source (Fianium WL-SC-400-15), with bandwidths of 450 to 2400 nm, was focused into a single mode fiber (1550BHP) using a X10 plan achromat objective (Olympus) with a numerical aperture of NA = 0.25. The single-mode fiber was aligned to the waveguide using a 3D stage (3-Axis NanoMax Stage) and monitored by a stereo microscope (Zeiss Stemi SV6) for precise alignment. The transmitted spectra were collected using a multimode fiber into a optical spectrum analyzer (Yokogawa 6370D) at a wavelength range of 1–1.7 μm and resolution of 1 nm.

RESULTS AND DISCUSSION

Molecular Overtone Transitions. Molecular vibration overtone transitions can be excited in near-IR. Each molecular vibration transition has a different probability to occur, which is expressed by the oscillator strength. The oscillator strength f is proportional to the square of electric dipole transition moment²⁶

$$f = \left(\frac{4\pi m_e \nu_{ij}}{3e^2 \hbar} \right) |\mu_{ij}|^2 \quad (1)$$

where m_e is the mass of an electron, \hbar is the reduced Planck constant, ν_{ij} is the frequency for transition from state i to state

j , and μ_{ij} is the electric dipole transition moment, which is defined as

$$\mu_{ij} = \langle i | \mu | j \rangle = \int \psi_i \mu \psi_j \, dr \quad (2)$$

where ψ is the wave function. The electric dipole moment μ is defined as

$$\mu = \mu_0 + \left(\frac{\partial \mu}{\partial r} \right)_0 r + \frac{1}{2} \left(\frac{\partial^2 \mu}{\partial r^2} \right)_0 r^2 + \dots \quad (3)$$

where μ_0 is the dipole moment at $r = 0$, where r is the displacement and 0 indicates that the derivatives are at the equilibrium bond length (detailed description of oscillator strength can be found in the Supporting Information). From eq S-10 in the Supporting Information, one can see that the probability of the overtone vibration is an order of magnitude smaller compared to the probability fundamental vibration,²² which makes it hard to identify. For this reason, here, we propose to enhance the overtone transition probability by the induced deflected Talbot effect on perforated optical waveguides with inclusions of cylindrical shape.

To investigate the influence of the inclusions on the Talbot effect, we study a Silicon-On-Insulator (SOI) nanostrip rib waveguide with 5 nm Ta₂O₅ overlayer, which acts as a capping layer, having a cluster made of cylindrical inclusions in the guiding layer, which is shown in Figure 1. We choose a square

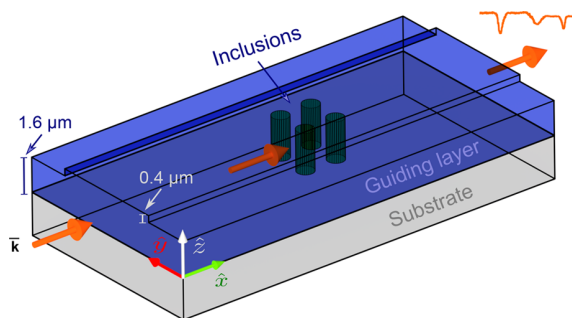


Figure 1. Schematic of the dielectric rib waveguide with a silicon guiding layer on the silica substrate with a cluster of inclusions of cylindrical shape.

configuration for the hole cluster due to the growing interest of quadrupers for different fundamental phenomena.²⁷ A cylindrical shape was chosen for the inclusions due to the easy fabrication process compared to other shapes. To observe the Talbot effect by a multimode interference, we modeled the waveguide with a height of 1.6 μm , nanostrip height of 400 nm, and inclusion diameter of 1.12 μm , as shown in Figure 1.

Using Lumerical FDTD software, we modeled the waveguide when the inclusions are embedded in different media: air and weakly absorbing media of *N*-methyl aniline (NMA) molecule.²⁸ A Gaussian beam, with a wavelength of 1.5 μm , radius of 4.75 μm , and divergence angle of 0.13 rad, was launched into the waveguide. The inclusions were engraved at a distance of 20 μm from the input facet. We explored the conditions for the deflected Talbot regime in x - y and x - z waveguide planes and its influence on molecular overtone transitions. Due to the propagation of a number of modes in a multimode waveguide, a wavefront replicates the periodic perturbation pattern along the propagation. When the dielectric perturbation occurs in a waveguide, some of the

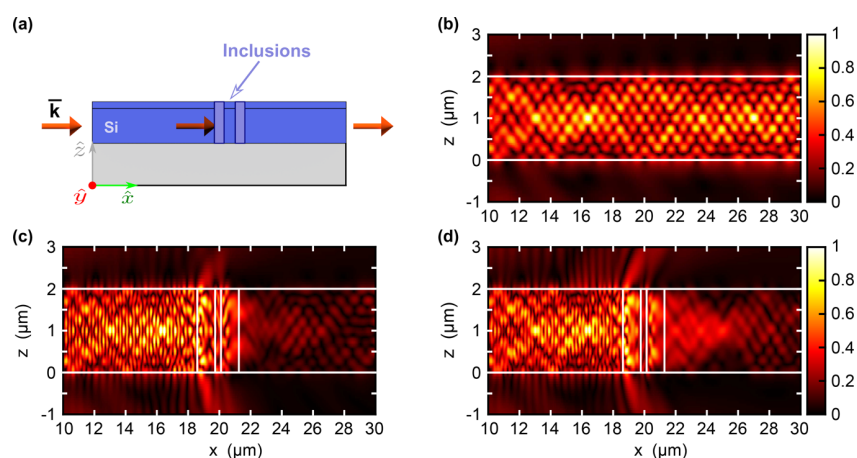


Figure 2. (a) Schematic of the cross section in the center of the waveguide, x - z plane ($y = 0 \mu\text{m}$). Evolution of the electric field when the waveguide was embedded in (b) air without inclusions, (c) air with inclusions, and (d) *N*-methylaniline, $n_{\text{NMA}} = 1.5712 + i8.931 \times 10^{-5}$, with inclusions.

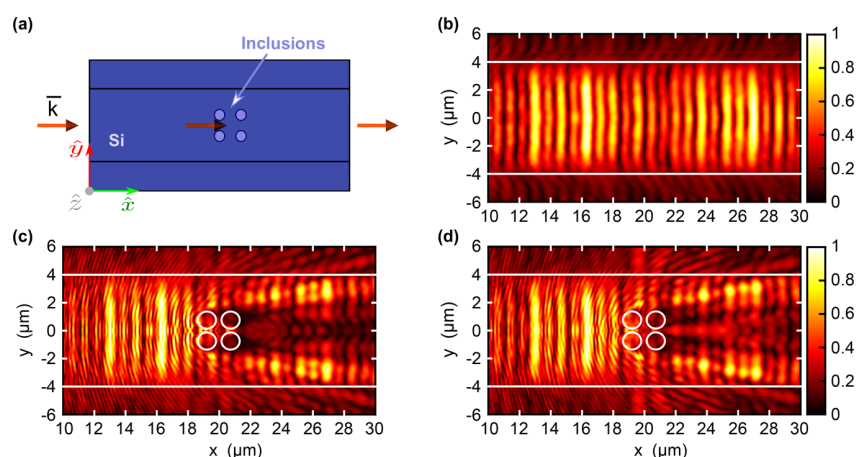


Figure 3. (a) Schematic of the cross section in the center of the waveguide, x - y plane ($z = 1 \mu\text{m}$). Evolution of the electric field when the waveguide was embedded in (b) air without inclusions, (c) air with inclusions, and (d) *N*-methylaniline, $n_{\text{NMA}} = 1.5712 + i8.931 \times 10^{-5}$, with inclusions.

power transfers to other modes, which creates the deflected Talbot effect.

First, we investigated the influence of the inclusions at the x - z plane of the waveguide. Figure 2a shows a schematic cross section in the center of the waveguide at the x - z plane. Due to the multimode interference, a self-imaging Talbot effect occurs in the silicon rib waveguide (Figure 2b). When the cylindrical inclusion cluster is placed inside the core, the deflected Talbot effect (Figure 2c,d) occurs when the guiding layer is embedded in air and in weakly absorbing medium with dispersion of *N*-methylaniline,^{24,28} respectively, which creates perturbation along the propagation direction of the waveguide. Next, we investigated the influence of the inclusions at the x - y plane of the waveguide. Figure 3a shows a schematic cross section in the center of the waveguide at the x - y plane. Figure 3b shows the Talbot effect in the silicon rib waveguide as a deformation of the field along the propagation. A perturbation appears along the propagation direction in the waveguide (Figure 3c,d) caused by the introduced inclusion cluster in the guiding layer embedded in air and in *N*-methylaniline, respectively. We notice a leakage beyond the waveguide strip confinement. Figures 2 and 3 show that some power transfers to the other

modes and the Talbot effect becomes deflected due to the dielectric perturbation of cylindrical shape (the evolution of the guided modes is shown in the Supporting Information).

For the experiment, we first fabricated and characterized the silicon rib waveguides. Figure 4a shows a scanning electron micrograph image of fabricated rib waveguides (top view) without inclusions. Next, the Talbot effect was deflected by the cylindrical inclusion cluster milled into the guiding layer with a focused ion beam (FIB) with a depth of 2 μm and radius of 580 nm. Figure 4b shows a scanning electron micrograph image of the zoomed area on the fabricated inclusion cluster (top view). The waveguides were characterized and tested using the inline waveguide measurement setup, as described in Experimental Section. Figure 4c shows a photograph of the inline setup with a fiber in-coupled rib waveguide aligned on the 3D stage. Fiber-out is collecting the output signal from the waveguide into the optical spectrum analyzer (OSA) (not shown).

To further explore the influence of the deflected Talbot regime on the overtone molecular absorption on the waveguide, we constructed the experimental setup shown in Figure 5a. We used red light of 80 mW. Therefore, partially,

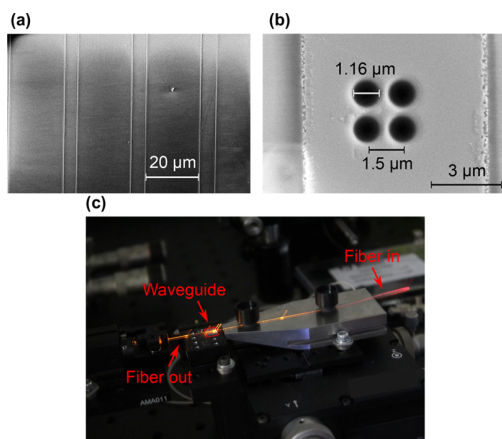


Figure 4. (a) Scanning electron microscopy (SEM) image of the rib waveguide. (b) Scanning electron microscopy (SEM) image of the fabricated inclusions on the rib waveguide. (c) Photograph of the inline experimental setup.

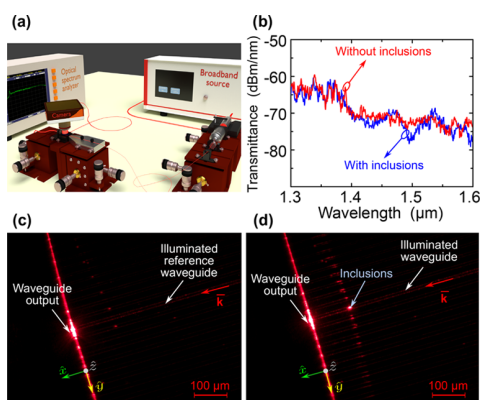


Figure 5. (a) Artistic impression of the experimental setup. (b) Measured transmittance spectra with OSA on the reference waveguide (red curve) and on the waveguide with a cylindrical inclusion cluster (blue curve). Note, both waveguides were embedded in *N*-methylamine medium. Top view of the waveguides captured with an optical microscope. (c) Reference waveguide. (d) Waveguide with fabricated inclusions.

such high-power light can be guided in the waveguide. It allows for the visualization of the waveguide lines and facilitates the alignment. Next, a broadband laser source was coupled to a single-mode fiber (SMF1550). The fiber was placed on a piezo-electric stage for precise and accurate inspection. The output signal was collected by a multimode fiber into an optical spectrum analyzer (OSA). We dropped 12 μL of *N*-methylamine onto the inclusion cluster shown in Figure 4c, resulting in the spectrum shown in Figure 5b (blue curve). For comparison, the laser was coupled to the reference waveguide (with no inclusions) with *N*-methylamine, resulting in the spectrum shown in Figure 5b (red curve). Figure 5c,d shows the upper view of the illuminated waveguide.

Figure 5b shows the transmittance spectrum of *N*-methylamine on the rib waveguide with and without inclusions at a broad wavelength range of 1.3–1.6 μm . The absorption of the N–H bond in *N*-methylamine is clearly seen around 1.5 μm on the waveguide with the inclusions. The absorption of *N*-methylamine when dripped onto the waveguide surface and filled in the inclusions is approximately

3.5 dB compared to dripped *N*-methylamine on a waveguide without the inclusions. It shows that in the deflected Talbot regime caused by the inclusions, we enhance the absorption effect of the *N*-methylamine probe molecule. Figure 5d shows the far-field scattering effect caused by the cylindrical inclusions compared to the scattering in the reference waveguide, as shown in Figure 5c, which fits the simulation results shown in Figure 3b,d.

We noticed that dielectric perturbations such as cylindrical holes enhance the absorption when the hole diameter is comparable to the incident wavelength. This can be explained by the scattering effect.

2D Scattering from a Cylinder Embedded in the Waveguide Core. The enhanced absorption of *N*-methylamine overtones can be explained by the multiple scattering events.^{28,29} One can explain the resonant elastic scattering of light by a chain of coherent absorption and re-emission events. Simply put, the photons are re-emitted in random directions because the wave vector is not conserved by the system for the lack of translational symmetry. The resonant scattering results in a significant increase in the mean trajectory of photons travelling through the guide. However, the actual scattering of a waveguide mode by a finite cylinder with a height of $H \approx \lambda$ and diameter of $D \approx \lambda$ cannot be solved analytically. Therefore, for describing the scattering effect by cylinders in the waveguide core, we will ignore the height restriction of the cylinder and illuminate it with a planar wave.

In the case of TE mode when the electric field is parallel to the xz plane, the scattered fields of a single cylinder (shown in Figure 6a) are defined as³⁰

$$\mathbf{E}_s = - \sum_{n=-\infty}^{\infty} E_n [b_{nl} \mathbf{N}_n^{(3)} + ia_{nl} \mathbf{M}_n^{(3)}] \quad (4)$$

$$\mathbf{H}_s = i \frac{k}{\omega\mu} \sum_{n=-\infty}^{\infty} E_n [b_{nl} \mathbf{M}_n^{(3)} + ia_{nl} \mathbf{N}_n^{(3)}] \quad (5)$$

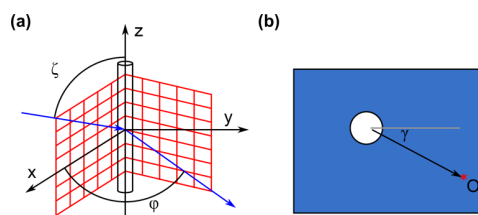


Figure 6. (a) Long cylinder illuminated by a plane wave. (b) Top view of the cylindrical hole.

where $E_n = E_0 (-i)^n / (k \sin \zeta)$, and $\mathbf{M}_n^{(3)}$ and $\mathbf{N}_n^{(3)}$ are the proper cylindrical vector harmonics,³⁰ which are given by

$$\mathbf{M}_n^{(3)} = \nabla \times (\hat{z} \psi_n) \quad (6)$$

$$\mathbf{N}_n^{(3)} = \frac{\nabla \times \mathbf{M}_n}{k} \quad (7)$$

where ψ_n is the generation function, which is defined as

$$\psi_n = H_n^{(1)}(kr \sin \zeta) e^{in\phi} e^{-ikz \cos \zeta} \quad (8)$$

where k is the wavenumber and $H_n^{(1)}$ is the Hankel function of the first kind, $H_n^{(1)} = J_n + iY_n$.

Using the continuity equations for E and H at the cylinder boundary ($r = a$), we obtain the two coefficients

$$a_{nl} = \frac{C_n V_n - B_n D_n}{W_n V_n + i D_n^2}$$

$$b_{nl} = \frac{W_n B_n + i C_n D_n}{W_n V_n + i D_n^2}$$

where the auxiliary functions are defined as

$$B_n = \xi [m^2 \xi J'_n(\eta) J_n(\xi) - \eta J_n(\eta) J'_n(\xi)]$$

$$C_n = n \cos(\zeta) J_n(\eta) J_n(\xi) \left(\frac{\xi^2}{\eta^2} - 1 \right)$$

$$D_n = n \cos(\zeta) \eta J_n(\eta) H_n^{(1)}(\xi) \left(\frac{\xi^2}{\eta^2} - 1 \right)$$

$$W_n = i \xi [\eta J_n(\eta) H_n^{(1)'}(\xi) - \eta H_n^{(1)}(\xi) J'_n(\eta)]$$

$$V_n = \xi [m^2 \xi J'_n(\eta) H_n^{(1)'}(\xi) - \eta H_n^{(1)'}(\xi) J'_n(\eta)]$$

and

$$\xi = ka \sin \zeta \quad \eta = ka \sqrt{m^2 - \cos^2(\zeta)}$$

where m is the relative refractive index of the medium filling the cylinder ($m = \frac{n_n + ik_n}{n_{wg}}$), and a is the cylinder radius.

In the case of a waveguide, the incident illumination is at normal incident to the inclusions ($\zeta = 90$); hence, a_{nl} is equal to zero. Therefore, b_{nl} can be calculated as

$$b_{nl} = \frac{J_n(mx) J'_n(x) - m J'_n(mx) J_n(x)}{J_n(mx) H_n^{(1)'}(x) - m J'_n(mx) H_n^{(1)}(x)} \quad (9)$$

For a finite cylinder, the correction factor is given by³¹ $f_c = \frac{2 \sin(kLA)}{kLA}$, where $A = \cos \zeta + \sin \theta \cos \phi$ and L is half of the cylinder length. This factor provides the spectral correction that depends on the cylinder length. However, it does not consider a space dependence of the field along the cylinder axes.

Using this simplified model, we can estimate the effect of the inclusion cluster. Using a single scattering model, the scattered field at an arbitrary point O is described as the sum of scattered field of each hole.

$$\mathbf{E}_{s(t)} = \sum_{n=1}^4 \mathbf{E}_{sn}(\gamma_n, |\mathbf{r}_O - \mathbf{r}_n|) \quad (10)$$

where n is the hole number and γ_n is the angle from the hole to point O .

The scattered field $\mathbf{E}_{s(t)}$ from the whole cluster of inclusions leads to the enhanced absorption when the hole diameter is comparable to the incident wavelength. The scattering transfers energy to the high-order modes, which have larger interaction with the surrounding. The scattering enhances the sensitivity of the waveguide, allowing us to identify the unique absorption lines of the molecule.

CONCLUSIONS

In conclusion, we have presented a waveguide system experiencing the deflected Talbot effect due to the appearance

of perturbations of cylindrical shape in the waveguide core embedded in weakly absorbing medium N -methyl aniline.²⁸ We fabricated the waveguides on the SOI platform and milled inclusions in them using the FIB technique. We found that the deflected Talbot effect on a waveguide enhances the absorption of molecular transition overtones. Specifically, the absorption line of the N–H bond of N -methyl aniline excited around 1.5 μm experienced a drop of 3.5 dB as compared to unperturbed by the inclusion waveguide. In addition, we noticed that dielectric perturbations such as cylindrical holes enhance the absorption when the hole diameter is comparable to the incident wavelength due to the scattering effect. This paves the way for integrated spectrometers in which the enhancement of the weak absorption occurs due to the perturbation in the waveguide core.

ASSOCIATED CONTENT

Supporting Information

The Supporting Information is available free of charge at <https://pubs.acs.org/doi/10.1021/acssensors.0c00325>.

Oscillator strength of overtones and fundamental modes, evolution of guided mode, and Figures S-1–S-4 (PDF)

AUTHOR INFORMATION

Corresponding Author

Alina Karabchevsky – School of Electrical and Computer Engineering and Ilse Katz Institute for Nanoscale Science & Technology, Ben-Gurion University of the Negev, Beer-Sheva 8410501, Israel; orcid.org/0000-0002-4338-349X; Email: alinak@bgu.ac.il

Author

Aviad Katiyi – School of Electrical and Computer Engineering and Ilse Katz Institute for Nanoscale Science & Technology, Ben-Gurion University of the Negev, Beer-Sheva 8410501, Israel; orcid.org/0000-0002-7924-9065

Complete contact information is available at: <https://pubs.acs.org/doi/10.1021/acssensors.0c00325>

Notes

The authors declare no competing financial interest.

ACKNOWLEDGMENTS

This work has been supported by Israel Innovation Authority within KAMIN program Grant No. 69073. The authors acknowledge Dr. Ioseph Gurwich for fruitful discussion.

REFERENCES

- (1) Yin, R.; Jiang, X.; Yang, J.; Wang, M. Structure with improved self-imaging in its graded-index multimode interference region. *J. Opt. Soc. Am. B* **2002**, *19*, 1301–1303.
- (2) Khalil, D.; Yehia, A. Two-dimensional multimode interference in integrated optical structures. *J. Opt. Soc. Am. B* **2003**, *6*, 137.
- (3) Ota, M.; Sumimura, A.; Fukuhara, M.; Ishii, Y.; Fukuda, M. Plasmonic-multimode-interference-based logic circuit with simple phase adjustment. *Sci. Rep.* **2016**, *6*, 24546.
- (4) Lierstuen, L.; Sudbo, A. 8-channel wavelength division multiplexer based on multimode interference couplers. *IEEE Photonics Technol. Lett.* **1995**, *7*, 1034–1036.
- (5) Wan, N. H.; Meng, F.; Schröder, T.; Shiue, R.-J.; Chen, E. H.; Englund, D. High-resolution optical spectroscopy using multimode interference in a compact tapered fibre. *Nat. Commun.* **2015**, *6*, 7762.

- (6) Peruzzo, A.; Laing, A.; Politi, A.; Rudolph, T.; O'Brien, J. L. Multimode quantum interference of photons in multiport integrated devices. *Nat. Commun.* **2011**, *2*, 224.
- (7) Geints, Y. E.; Minin, O. V.; Minin, I. V.; Zemlyanov, A. A. Self-images contrast enhancement for displacement Talbot lithography by means of composite mesoscale amplitude-phase masks. *J. Opt. Soc. Am. B* **2020**, *22*, No. 015002.
- (8) Talbot, H. F. LXXVI. Facts relating to optical science. No. IV. *London Edinburgh Phil. Mag. J. Sci.* **1836**, *9*, 401–407.
- (9) Rayleigh, L. *London Edinburgh Phil. Mag. J. Sci.* **1881**, *11*, 196–205.
- (10) Bryngdahl, O. Image formation using self-imaging techniques. *J. Opt. Soc. Am.* **1973**, *63*, 416–419.
- (11) Ulrich, R. Light-propagation and imaging in planar optical waveguides. *Nouv. Rev. Opt.* **1975**, *6*, 253.
- (12) Praxmeyer, L.; Wódkiewicz, K. Talbot effect in cylindrical waveguides. *Opt. Commun.* **2006**, *268*, 215–225.
- (13) Soldano, L. B.; Pennings, E. C. M. Optical multi-mode interference devices based on selfimaging: principles and applications. *J. Lightwave Technol.* **1995**, *13*, 615–627.
- (14) Bachmann, M.; Smit, M.; Besse, P.; Gini, E.; Melchior, H.; Soldano, L. Polarization-insensitive low-voltage optical waveguide switch using InGaAsP/InP four-port Mach-Zehnder interferometer. In *Conference on Optical Fiber Communication/International Conference on Integrated Optics and Optical Fiber Communication*; OSA Publishing: 1993, p TuH3.
- (15) Agrawal, N.; Weinert, C.; Ehrke, H.-J.; Mekonnen, G.; Franke, D.; Bornholdt, C.; Langenhorst, R. Fast 2 x 2 Mach-Zehnder optical space switches using InGaAsP-InP multi-quantum-well structures. *IEEE Photonics Technol. Lett.* **1995**, *7*, 644–645.
- (16) Zucker, J.; Jones, K.; Chiu, T.; Tell, B.; Brown-Goebeler, K. Strained quantum wells for polarization-independent electrooptic waveguide switches. *J. Lightwave Technol.* **1992**, *10*, 1926–1930.
- (17) Jenkins, R. M.; Devereux, R. W. J.; Heaton, J. M. A novel waveguide Mach-Zehnder interferometer based on multimode interference phenomena. *Opt. Commun.* **1994**, *110*, 410–424.
- (18) Katiyi, A.; Karabchevsky, A. Si Nanostrip Rib-Waveguide for On-Chip Broadband Molecular Overtone Spectroscopy in Near-Infrared. *ACS Sensors* **2018**, *3*, 618–623.
- (19) Wang, J.; Jin, Y.; Zhao, Y.; Dong, X. Refractive index sensor based on all-fiber multimode interference. *Optik* **2013**, *124*, 1845–1848.
- (20) Mayeh, M.; Viegas, J.; Srinivasan, P.; Marques, P.; Santos, J. L.; Johnson, E. G.; Farahi, F. Design and fabrication of slotted multimode interference devices for chemical and biological sensing. *J. Sen.* **2009**, *2009*, 1.
- (21) Katiyi, A.; Zorea, J.; Halstuch, A.; Elkabets, M.; Karabchevsky, A. Surface roughness-induced absorption acts as an ovarian cancer cells growth sensor-monitor. *Biosens. Bioelectron.* **2020**, *161*, 112240.
- (22) Stuart, B. *Infrared spectroscopy: Fundamentals and applications*; John Wiley & Sons, Ltd.: Sussex, 2004.
- (23) Struve, W. S. *Fundamentals of molecular spectroscopy*; Wiley: New York, 1989.
- (24) Katiyi, A.; Karabchevsky, A. Figure of merit of all-dielectric waveguide structures for absorption overtone spectroscopy. *J. Lightwave Technol.* **2017**, *35*, 2902–2908.
- (25) Borovkova, O. V.; Ignatyeva, D. O.; Sekatskii, S. K.; Karabchevsky, A.; Belotelov, V. I. High-Q surface electromagnetic wave resonance excitation in magnetophotonic crystals for super-sensitive detection of weak light absorption in the near-infrared. *Photonics Res.* **2020**, *8*, 57–64.
- (26) Atkins, P. W.; Friedman, R. S. *Molecular quantum mechanics*; Oxford University Press: 2011.
- (27) Terekhov, P. D.; Evlyukhin, A. B.; Redka, D.; Volkov, V. S.; Shalin, A. S.; Karabchevsky, A. Magnetic Octupole Response of Dielectric Quadrumers. *Laser Photonics Rev.* **2020**, 1900331.
- (28) Karabchevsky, A.; Kavokin, A. V. Giant absorption of light by molecular vibrations on a chip. *Sci. Rep.* **2016**, *6*, 21201.
- (29) Karabchevsky, A.; Katiyi, A.; Bin Abdul Khudus, M. I. M.; Kavokin, A. V. Tuning the Near-Infrared Absorption of Aromatic Amines on Tapered Fibers Sculptured with Gold Nanoparticles. *ACS Photonics* **2018**, *5*, 2200–2207.
- (30) Bohren, C. F.; Huffman, D. R. *Absorption and scattering of light by small particles*; John Wiley & Sons: 2008.
- (31) Hulst, H. C.; van de Hulst, H. C. *Light scattering by small particles*; Courier Corporation: 1981.

2.3 Surface roughness-induced absorption acts as an ovarian cancer cells growth sensor-monitor

The third step in my research was to investigate a different method for enhancing sensitivity by decreasing the confinement of the mode. To this end, I studied microfiber for enhancing sensitivity for monitoring cancer cells treatment in-vitro [47].

Ovarian cancer is one of the leading causes of death in women. Late diagnosis is one of the major causes for [48, 49]. Optical fiber can be used for sensing. To use optical fiber for sensing, the fiber needs to be tapered, creating a microfiber region that acts as the sensing region. In this region, the fiber diameter is smaller and the confinement of the fiber decreases [50] causing an increase in the penetration depth of the evanescent field. This improves the sensitivity of the fiber.

I investigated the vibration absorption of untreated and treated ovarian cancer cells using a tapered fiber. A conventional single-mode fiber was tapered to a diameter of $2.5 \mu\text{m}$. In this microfiber region, the evanescent tail appears outside the fiber and the small diameter increases the penetration depth of the evanescent field. Both enhance sensitivity. In the experiment, a broadband laser source was coupled in the tapered fiber. $12 \mu\text{l}$ of the cancer samples were dropped on a Teflon spacer, which acts as a liquid reservoir due to its hydrophobic property. The cancer cells were treated with different concentrations of the medicine. The Teflon was softly slid to the microfiber region and the transmission was collected to an optical spectrum analyzer. I found that the absorption was higher compared to the simulation with the same microfiber diameter. This is caused by the random roughness of the microfiber that occurs in the fabrication process.

From these results, I concluded that the random roughness of the microfiber surface not only causes scattering losses, but even enhances sensitivity by increasing the penetration depth of the evanescent field.



Surface roughness-induced absorption acts as an ovarian cancer cells growth sensor-monitor

Aviad Katiyi^{a,b}, Jonathan Zorea^c, Aviran Halstuch^{a,b}, Moshe Elkabets^c, Alina Karabchevsky^{a,b,*}

^a School of Electrical and Computer Engineering, Ben-Gurion University of the Negev, Beer-Sheva, 8410501, Israel

^b Ilse Katz Institute for Nanoscale Science & Technology, Ben-Gurion University of the Negev, Beer-Sheva 8410501, Israel

^c The Shraga Segal Department of Microbiology, Immunology and Genetics, Faculty of Health Sciences, Ben-Gurion University of the Negev, Beer-Sheva, 8410501, Israel

ARTICLE INFO

Keywords:

Cancer
Overtones
Microfiber
Sensor
Near-infrared
In-vitro

ABSTRACT

Uncontrolled growth of ovarian cancer cells is the fifth leading cause of female cancer deaths since most ovarian cancer patients are diagnosed at an advanced stage of metastatic disease. Here, we report on the sensor for monitoring the cancer treatment efficiency in real-time. We measure the optical interaction between the evanescent fields of microfiber and ovarian cancer inter-cellular medium at different treatment stages. Spectral absorption signatures are correlated with optical micrographs and western blot tests. We found that the treatment of tumor cells with induces both cells growth arrest and alter the spectral lines in a dose-dependent manner. These observations are mediated by surface roughness out of silica glass material, form an essential step toward the development of early detection of response to cancer therapy.

1. Introduction

Ovarian cancer is the fifth leading cause of female cancer deaths due to late stage diagnoses (Fishman and Bozorgi, 2002; Lengyel, 2010), while diagnosis at earlier stages of ovarian cancer has a 5-year relative survival rate of 92% (Noone et al., 2018). However, most ovarian cancer patients are diagnosed at an advanced stage of metastatic disease, as the tumor spreads into the peritoneum. This aggressive disease is incurable and the survival rate of such a patient is as low as 30%. This poor survival rate is primarily related to recurrent disease of chemotherapy-resistant tumors, hence, adjustment of an appropriate second and third line of chemotherapy (or targeted therapy) is required to improve the survival rate. Currently, there are no clinical biomarkers to prioritize treatment for these patients (except of BRCA1/2 mutation (Kurian et al., 2010; Lee et al., 2013)), and treatment efficiency is monitored weeks after the initial treatment. Application of a system that will record therapy efficiency hours or days after treatment will be a major milestone in the care of ovarian cancer patients.

The conventional procedure of monitoring cancer treatment efficiency is performed with harmful methods such as positron emission tomography (PET) and computed tomography (CT) scan simultaneously (Beyer et al., 2000; Johnson et al., 2016; Fischer et al., 2009; Pelosi et al., 2004). The PET scan gives information about the activity of the cell using a radioactive tracer, while the CT scan gives a 3-dimensional image of the body using X-ray. Simultaneous PET-CT

monitoring provides an accurate information about the tumor morphology and malignancy state (Schäfers and Stegger, 2008; Stegger et al., 2007). However, this not-affordable, bulky, and cumbersome imaging equipment is both harmful and not suitable for bedside monitoring; it is not always available and requires qualified personnel to operate.

Silica glass is an important material used in microelectronics due to its insulating properties. However, this most complex, most abundant material and widely used in optical systems is susceptible to surface alterations. Therefore, it is long being considered inappropriate for bedside healthcare applications. Yet, it is among the most important materials used in science and technology due to its robustness, chemical resistance, insulating properties and biocompatibility (Kotz et al., 2017; Geisler et al., 2019; Paget, 1924). Due to its transparency to light at telecommunication wavelengths (Arumugam, 2001; Midwinter, 1976; Palais, 1988), optical fibers composed of silica have been explored and utilized since the previous decade for light signal transfer (Suematsu, 1983; Okoshi, 1987). Despite wide usage of silica glass fibers for sensing (Chow et al., 2018; Soto et al., 2016; Caucheteur et al., 2016; Wan et al., 2015), biomedical and healthcare applications (Fried and Irby, 2018; Rao et al., 1998; Peterson and Vurek, 1984; Rao et al., 1997; Motz et al., 2004), their contribution to cancer treatment efficiency is still elusive.

Despite the wide body of research regarding optical imaging and sensing techniques for monitoring absorption changes of tumor cells

* Corresponding author.

E-mail address: alinak@bgu.ac.il (A. Karabchevsky).

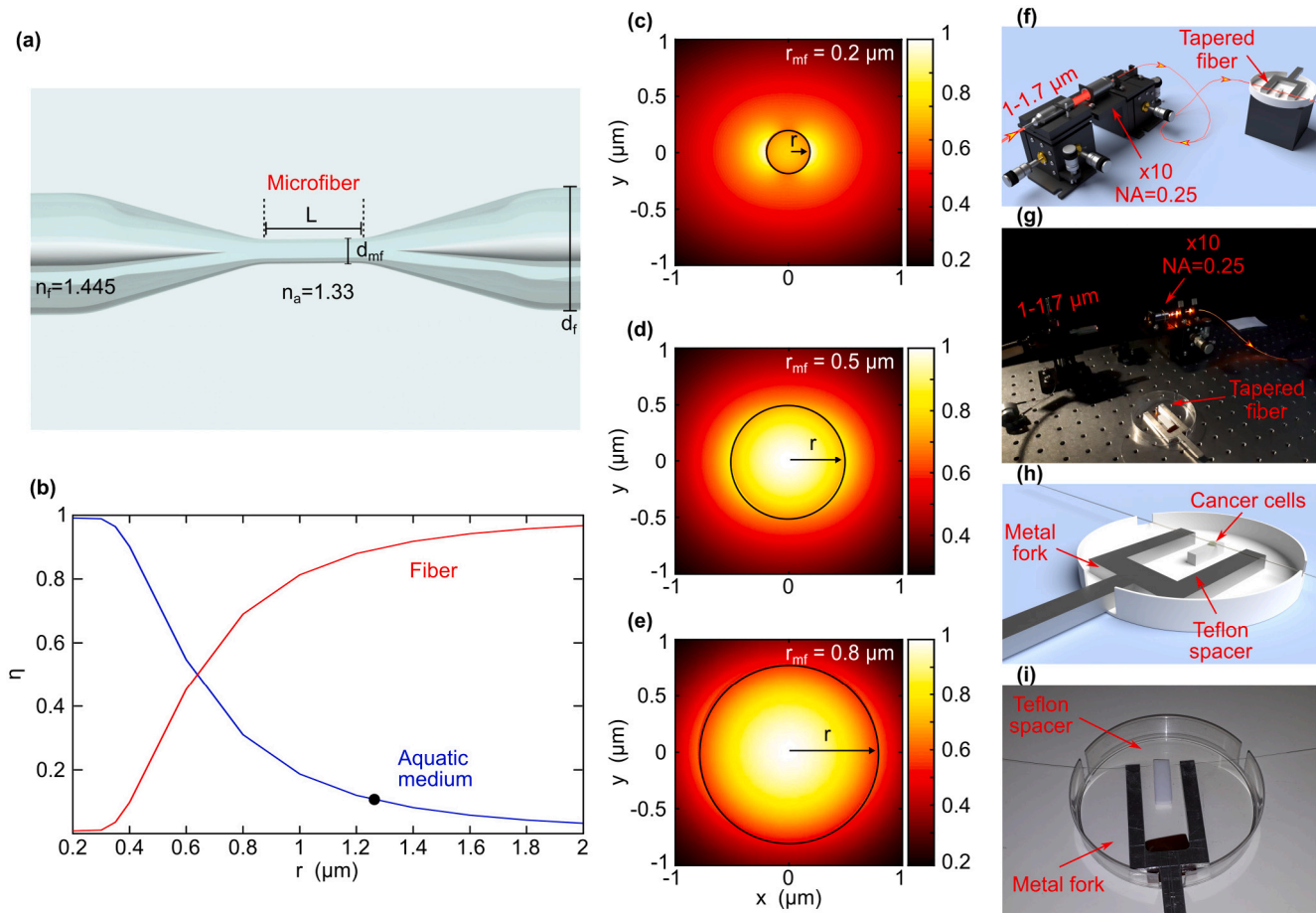


Fig. 1. Experimental set-up for overtones absorption spectroscopy from silica glass microfibers. (a) Schematic drawing of a tapered fiber structure (not to scale). (b) Calculated fraction of power at wavelength of $1.5 \mu\text{m}$, in the fiber (red) and in the analyte (blue) with index of 1.33, over the total power carried by the guided modes. $\sim 15\%$ of the total power in the analyte is indicated by the dot. Calculated normalized electric field (EF) distributions for various microfiber radii: (c) $r_{mf} = 0.2 \mu\text{m}$, (d) $r_{mf} = 0.5 \mu\text{m}$ and (e) $r_{mf} = 0.8 \mu\text{m}$. (f) Schematic drawing of the experimental set-up with broadband laser source coupled to a single-mode fiber using an $\times 10$ objective. (g) Photograph of the experimental setup. (h) Schematic drawing of the tapered fiber sensing device. (i) Photograph of the tapered fiber sensing device. (For interpretation of the references to color in this figure legend, the reader is referred to the web version of this article.)

(Mackanos and Contag, 2010; Chang et al., 2005; Mahadevan-Jansen et al., 1998; Sung et al., 2003) the contribution of surface topology in terms of surface roughness on optical microfibers was never explored in cancer media. For this, first we design the particular microfiber landscape by solving Maxwell equations numerically with the help of the simulator that we built, then we fabricate the microfiber, and finally, we test the microfiber in cellular media of treated and untreated cells.

In this work, we use the detection of overtone lines related to the inter-cellular cancer medium in near-infrared (NIR) in order to monitor the cancer cells treatment efficiency. Infrared spectroscopy, commonly called vibration or overtone spectroscopy, is an important analytical technique and provides information on molecular signatures in different states of matter: liquid, solid, or gas (Struve, 1989). Even though the NIR region has benefits of affordable sources and detectors developed to operate at telecommunication window, the absorption cross-section of molecular vibrations overtones is order of magnitude smaller compared to the fundamental vibrations of the same degree of freedom (Suart, 2004) making the detection of overtones at NIR spectrum challenging.

Here, we report the results of an all-optical proof-of-concept device shown on Fig. 1a for monitoring of cancer cells treatment. Based on our pioneering works on molecular vibrations overtones detection in near-infrared (NIR) (Karabchevsky and Kavokin, 2016; Katiyi and Karabchevsky, 2017, 2018; Karabchevsky et al., 2018; Dadadzhyanov et al., 2018; Karabchevsky and Shalabney, 2016; Borovkova et al.,

2019; Dadadzhyanov et al., 2019; Borovkova et al., 2020), we relate the absorption bands to the morphological change of cancer cells. To this end, we designed and tested the nanophotonic device to measure the overtones vibration spectra of intercellular medium of treated and untreated isolated ovarian tumor cells with different concentrations of the PI3K inhibitor. We discovered that the fingerprint signatures of the cancer cells viability could be detected from the intercellular medium. We also designed and tested the nanophotonic device to probe the overtones vibration spectrum of intercellular medium while monitoring the modification of cancer cells under selective pressure of therapy. We noticed that the enhanced evanescent field of the microfiber allows monitoring the tumors cell viability. Our results open up a plethora of precise, miniature, and portable devices for in-vitro healthcare applications and for future in-vivo applications. The bedside applications of the proposed fiber probe will involve the extraction of tumor cells from patient's ascites pre- and post-treated with chemotherapy. The efficacy of the therapy will be then monitored in-vitro with the fiber.

2. Material and methods

2.1. Fiber simulation

The fiber modes simulation was performed using COMSOL Multiphysics FEM (Finite Element Method).

2.2. Fabrication of the sensing device

We tapered the single-mode fiber (SMF-28) to approximately 2.5 μm diameter using a commercial Vytran GPX-3000 tapering system. First, we removed the acrylate polymer coating from the tapering area. The tapering was done in two step process. At the first stage the fiber was tapered from a diameter of 125 μm to a diameter of $\sim 15 \mu\text{m}$. Then, the fiber was tapered from a diameter of $\sim 15 \mu\text{m}$ to a diameter of $\sim 2.5 \mu\text{m}$. We glued the tapered fiber on both sides with Epoxy glue to a metal fork, which we designed and fabricated for robustness. We placed a Teflon spacer under the tapered fiber. We used the Teflon spacer as a liquid reservoir for holding the cancer cells due to the Teflon's surface tension.

2.3. Cell cycle

Cells and growth medium were collected, centrifuged for 10 mins at 4 $^{\circ}\text{C}$, then a pellet was fixed using 70% ice-cold ethanol and stored at -20°C . Before the read, the pellet was washed twice with cold 1X PBS, treated for 30 mins at 37 $^{\circ}\text{C}$ with 100 μl of RNase solution (100 $\mu\text{g}/\mu\text{l}$), and stained in the dark for 20 mins with 200 μl Propidium iodide solution (100 $\mu\text{g}/\text{ml}$). The cell phase was analyzed using BD FACSCANTO II.

2.4. Cell lines and chemical compounds

Ovarian cancer cell line (IGROV1) obtained from ATCC and maintained at 37 $^{\circ}\text{C}$ in a humidified atmosphere at 5% CO_2 , in RPMI-1640 medium, supplemented with 1% L-glutamine 200 mM, 100 units of penicillin and streptomycin and 10% fetal bovine serum. GDC0032 were purchase from MedChemExpress (HY-13898) and were dissolved in DMSO at a stock concentration of 10 mM. Cell were treated at a concentration of 50 nM. The cancer cells were removed from the plastic plate by trypsin, washed in PBS and suspended in UV-sterile water at concentration of $1 \cdot 10^6$ cells/ml.

2.5. Cancer cells imaging

The cancer cells were imaged using Carl Zeiss Inverted microscope Axio Observer 7 system.

2.6. Western blotting

Plates with cells were washed with cold PBS and suspended with cold lysis buffer containing phosphatase inhibitor cocktail (Stratech, B15001-BIT). Lysates were then centrifuged at 14 000 rpm for 10 mins at 4 $^{\circ}\text{C}$, and supernatants were collected and assayed for protein quantification using the Bradford protein assay (Biorad, 5000006). 1 mg/ml of quantified lysate were resolved on NuPAGE 4/12% Bis-Tris gels and transferred to PVDF membranes (Biorad, 1704157). Membranes were incubated for 1 h in 5% BSA in Tris-buffered saline (TBS)-Tween and then hybridized using the primary antibodies (P21, actin, AKT) in 5% BSA TBS-Tween. Horseradish peroxidase (HRP)-conjugated secondary antibodies (1:20000, GE Healthcare) were diluted in 5% BSA in TBS-Tween. Protein-antibody complexes were detected by chemiluminescence with ECL (Cyanagen) and imaged with a c300 azure camera system. SMOBIO-PM-2600 protein marker were used to analyze bend size.

2.7. Statistical analysis

The experiment was repeated at least three times. Statistical analysis was performed using GraphPad Prism software, presented as mean \pm SEM. For comparisons between conditions, Ordinary one-way ANOVA were used. Values of 0.05(*), 0.01(**), 0.001(***) and 0.0001(****) were considered statistically significant.

2.8. Experiment optical set-up

A broadband laser source (Fianium WL-SC-400-8-PP), with a wavelength range from 450 nm to 2400 nm, was coupled into a SMF (1550BHP) using Olympus plan achromat objective with NA 0.25 and magnification x10. The SMF was spliced to the tapered fiber using Fujikura 70 s fiber fusion splicer. Cancer volume of 12 μL and 4000 cells/ μL was dropped onto Teflon bulk and slid to the microfiber region. The transmittance spectra were collected into an optical spectrum analyzer (OSA, Yokogawa AQ6370) with a resolution of 1 nm and a sampling interval of 0.2 nm. The transmittance spectrum was measured from 1000 nm to 1700 nm.

3. Results and discussion

3.1. Numerical approach and method description

In order to find the optimal design, numerical investigations were performed before fabricating the device. The numerical model was built for the microfiber structure in which the light propagates due to the total internal reflection effect in direction of vector \vec{k} . The evanescent field, some fraction of the field propagated and decayed beyond the physical dimensions of the microfiber core, interacted with the studied aquatic medium. In a single-mode fiber (SMF), when the V-number is below 2.40541, only a small fraction of the power is carried in the evanescent field (Katiyi and Karabchevsky, 2017), and this affects the sensitivity of the sensor. When the V-number of the fiber is decreased, the confinement of the guided optical mode in the fiber core decreases as well (Agrawal, 2012) and more energy is guided in the cladding. Our calculations show that 70% of the power in the fiber core is guided for V-number of 2 and 20% of the power in the fiber core is guided for V-number of 1.

We designed our fibers such that the decreased confinement (Katiyi and Karabchevsky, 2017) of the optical mode increases the penetration depth of the guided light into the cellular medium by minimizing the V-number. This in turn, improved the interaction between the evanescent field and the analyte. To find the optimal fiber diameter, we calculated the fraction of the power carried by the evanescent field.

We built a simulator based on fine element method (FEM) algorithm implemented by COMSOL Multiphysics and solved Maxwell equations to study the device performance. Fig. 1b shows the fraction of the power (η) calculated according to Ref. (Katiyi and Karabchevsky, 2017) in the microfiber core and in the aquatic medium while varying the fiber radius. Fig. 1c shows the evolution of the guided modes in the fiber core as a function of the fiber radius. We notice that the smaller the diameter of the fiber, more light leaks beyond the fiber core into the medium in which the fiber is embedded. We calculated the normalized electric field distributions of a microfiber having core index of 1.445 embedded in aquatic medium with index of 1.33, for a wavelength of 1.5 μm . As the radius of the microfiber is reduced, the penetration depth of the evanescent tail increases (Fig. 1c–1e). Therefore, we fabricated a tapered fiber based on these insights; we heated and pulled an SMF with core diameter of $\sim 9 \mu\text{m}$ and cladding diameter of 125 μm to obtain a core diameter as small as $\sim 2.5 \mu\text{m}$ without a cladding. The fabricated fiber lead to an enhanced evanescent field, with $\sim 15\%$ of the total power, as marked by the dot on Fig. 1b. This reduced diameter allows for efficient probing of the analyte without sacrificing the entire power.

3.2. Biological test and spectral analysis

Spectroscopic experiments were performed in biological material of seeded ovarian tumor cells, IGROV-1 (Bénard et al., 1985), on the fiber. Nine fibers (Fig. 1f), monitored using an optical spectrum analyzer (OSA, Yokogawa AQ6370), were tested. Fig. 1g shows the designed handling tool with hydrophobic Teflon spacer. A broadband laser source (Fianium WL-SC-400-8-PP) was coupled into a single-mode

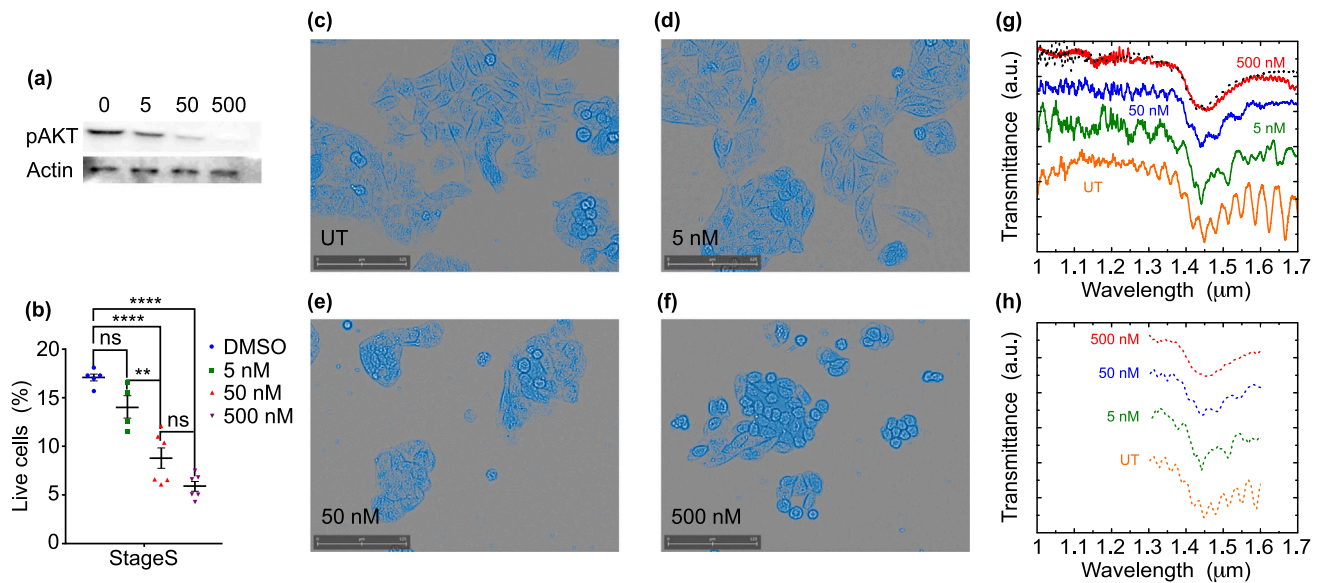


Fig. 2. (a) Western blot analysis of pAKT of IGROV-1 cells, treated with three different concentrations of GDC-0032 (5 nM, 50 nM and 500 nM) for 24 h, compared to the beta-actin level (3 repeats for each individual point). (b) Flow cytometry-based (FACS) analysis of the population in S phase in IGROV-1 cell line, 24 h after treatment with DMSO or 5 nM, 50 nM and 500 nM of GDC0032 (mean \pm S.E.M. $n \geq 4$, ** $P < 0.01$, **** $P < 0.001$). Optical micrographs of IGROV1 cells: (c) untreated and treated with different medicine concentrations (d) 5 nM, (e) 50 nM, and (f) 500 nM. (g) The transmittance of cancer cells with different concentrations of the medicine. Dotted curve shows the spectral response of healthy cells. (h) Numerical modeling results for microfiber with diameter of 2.5 μm and length of 2 mm embedded in medium of different concentration of the drug. (For interpretation of the references to color in this figure legend, the reader is referred to the web version of this article.)

fiber using an objective x10. The single-mode fiber was spliced with the tapered fiber and the output spectra were collected into an optical spectrum analyzer with resolution of 1 nm. We tapered a single-mode fiber to approximately 2.5 μm diameter and glued it to a metal handling tool as shown in Fig. 1h. Since the surface of the spacer is hydrophobic and can be used a liquid-reservoir, the sample was isolated within the tear-sized dimensions on Teflon. The tumor cells in buffer solution were dripped onto the spacer and the microfiber was immersed in the droplet of 12 μL . During the experiment, the near-infrared spectrum was monitored with time intervals of 30 s to observe the time dependent change of molecular overtones signatures. In addition, we treated the IGROV-1 cells with PI3K inhibitor, GDC-0032, to explore if such agent, which is known to induce tumor growth arrest (Zorea et al., 2018), also affects the absorption of molecular overtones indicating the change in cancer viability. The sensitivity of the device to response therapy was tested by treating the IGROV-1 tumor cells with three different concentrations of GDC-0032 (5 nM, 50 nM and 500 nM) for 24 h. Using western blot (Fig. 2a) and flow cytometry (Fig. 2b) methods, we confirmed a dose-dependent effect of GDC-0032 on IGROV-1 cells with a reduction of pAKT (Abbas and Dutta, 2009) and a reduction in S phase, respectively.

Fig. 2c shows optical image of untreated cancer cells while Fig. 2d–2f show treated cancer cells with 5 nM, 20 nM and 500 nM concentration of the GDC-0032 medicine. These images show that when the concentration of the GDC-0032 increases, the cells shrink and exhibit a decrease in their spatial distribution. Following these results, we tested the NIR spectral signature of cells under the same conditions. Fig. 2g shows the transmittance of the microfiber embedded in the intercellular medium of the cancer cells while the cells were treated with 5 nM, 50 nM and 500 nM concentration of the GDC-0032 medicine. The limit of detection was determined using three standard deviations and 20 repeats of signals for each individual point. As a control signal, we measured the untreated cancer cells. The signal of untreated cancer cells shows the features of fringes related to the interference effect of relatively big bio-entities surrounding the fiber. As the concentration of the GDC-0032 on the cancer cells increases, the interference disappears but the bifurcated absorption effect appears around 1500 nm — area associated with the N–H overtone bond (Karabchevsky and Kavokin, 2016; Karabchevsky et al., 2018; Karabchevsky and Shalabney, 2016;

Wheeler, 1959). This bifurcation effect is well defined for the concentration of the GDC-0032 of 5 nM and gets suppressed when the concentration of GDC-0032 is increased to 50 nM. Related optical images show the decrease in spatial distribution of the cells as the treatment changes from 5 nM to 50 nM.

Remarkably, the dip around 1450 nm in signals obtained when the tumor was treated with 5 nM and 50 nM is associated with the hydroxylic group (Wheeler, 1959). When the concentration of the GDC-0032 is as high as 500 nM, the bifurcation merges into one well-defined and smooth dip around 1450 nm. The corresponding optical image on Fig. 2f shows that the tumor cells are squeezed and their distribution is affected, supporting our assumption that the spectral feature for 500 nM medicine concentration shows the positive response to treatment. We noticed that while further increasing the concentration of the medicine, the signal remains identical to the signals from cells treated with 500 nM GDC-0032. Therefore, we conclude that 500 nM GDC-0032 inhibits cell proliferation, and prevents the tumor growth and distribution. This inhibition affects metabolic reaction and reduces the prevalence of the N–H bonds as well as the hydroxyl groups. To understand our results, we studied the disordered wave propagation in frame of coupled-mode theory. Assuming the unperturbed system and dispersion of drug-treated and untreated (UT) medium, the translational invariance defines the waveguide modes which we solve numerically. Fig. 2h shows the numerical solution of the wave equation in cylindrical coordinates with the boundary conditions of the microfiber having a diameter of 2.5 μm and an interaction length of 2 mm embedded in different media of treated and untreated cancer cells. Numerical results are in good agreement with experimental data. We note, that in the experiment the interaction length was 4 times smaller as compared to theoretical prediction. Specifically, interaction length of the microfiber 0.5 mm was fabricated while in the theory, the interaction length was considered as 2 mm to fit the experimental data. In the experiment, 4 times enhancement in absorption is observed as compared to the theoretical estimations. This remarkable observation can be interpreted as roughness-induced absorption due to the surface roughness of the fiber discussed below.

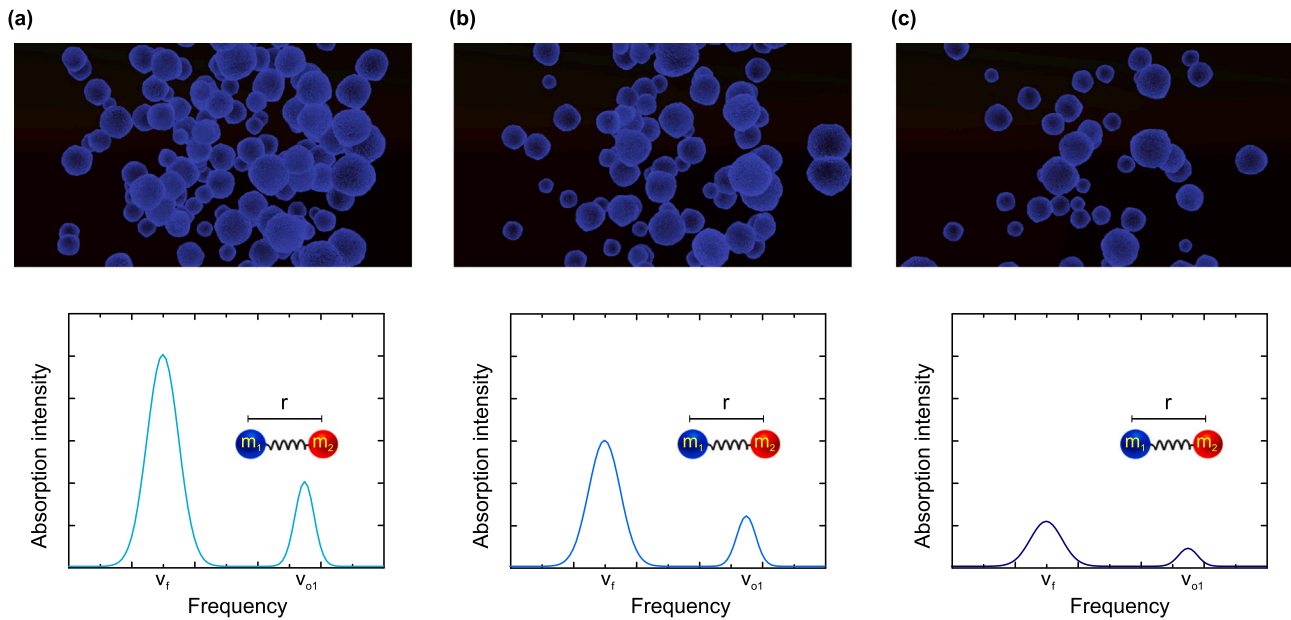


Fig. 3. Schematics of the oscillator mechanism when the cancer cells are under different treatment stages. Cellular spatial distributions (top) and the corresponding absorption intensities (bottom) for (a) low concentration of medicine, (b) medium concentration of medicine, and (c) optimal concentration of medicine — influence on cancer cells and metabolism. r designates the inter-atomic distance.

3.3. Scattering and oscillator mechanism

We note that the spatial distribution of the cancer cells has an influence on the spectral absorption signatures (Fig. 2). Fig. 2c–2f show that the concentration of the medicine during the treatment has influence on the density and distribution of the cancer cells. The cellular density affects the scattering mean free path l_{sc} , the distance until the light is scattered, which is defined as Lorenzo (2012):

$$l_{sc} = \frac{1}{\mu_s} \text{ [cm]} \quad (1)$$

with scattering coefficient μ_s with

$$\mu_s = \rho \sigma_{sc} \quad (2)$$

where ρ is the density of the particles and σ_{sc} is the scattering cross-section of a single particle.

In untreated cancer sample, the cancer cells are densely packed (Fig. 2c) which decreases the scattering mean free path. As a result, the scattering increases, which decreases the overall-transmission as shown in Fig. 2b (orange curve). For medicine concentration of 50 nM (Fig. 2g - blue curve), the distribution of the cancer cells is small (Fig. 2e) and therefore the scattering decreases, leading to the improvement in overall transmission, and thus the molecular signature of the medium can be identified.

The oscillator mechanism when the cancer cells are under different treatment stages is shown on Fig. 3, explains how the medicine terminates the metabolism and cellular growth. When the cells are treated with insufficient concentration of medicine, they experience dense spatial distribution with well-defined cellular boundaries Fig. 3a(top). The corresponding absorption intensity of the excited overtone is as high as shown in Fig. 3a(bottom).

Fig. 3b(top) shows lower spatial density of cells as compared to Fig. 3a(top), due to the increase in the concentration of the medicine leading to suppressed absorption intensity shown in Fig. 3b(bottom). Fig. 3c shows the influence of the high concentration of the medicine on the cancer cells leading to the reduced cellular volume, lower spatial density Fig. 3c(up) and corresponding suppressed absorption lines as expected. This effect can be interpreted as the roughness-induced enhanced absorption. Recent studies show that high index nanoparticles

with high index contrast between the particles and the medium in which these particles are embedded experience directional scattering effect (Terekhov et al., 2017, 2019a,b,c; Shamkhi et al., 2019). However here, the contrast between the scatters and the medium is very low.

3.4. Enhanced absorption and surface roughness influence

It is important to note that the surface roughness plays a crucial role in the observed effect of roughness-induced enhanced absorption. Ideally, the optical fiber is considered as having a smooth surface, also tapered fibers illuminated with external source show continuous and smooth boundary as shown in Fig. 4a (captured with x100 home-built magnification system). However, the heating-based tapering process, introduces surface roughness. To explore the effect of surface roughness, we switched off the external free-space illumination in home-built magnification system and coupled the light into the tapered fiber itself. Now, when the tapered fiber guides a light, the bright scattered spots can be observed (Fig. 4b). This is the evidence that the unbounded glass surface has a random surface roughness.

The surface roughness of the microfiber can be represented as a variation in the microfiber core radius. In the first approximation, the microfiber surface roughness can be explained by the Gaussian random field. The perturbation magnitude can vary and therefore, the amplitude of the electric field in guided and radiated modes changes contributing altogether to the surface sensitivity. The spectral power density $P(k)$ of the surface roughness can be expressed as Jackle and Kawasaki (1995):

$$P(k) = \frac{k_B T}{\alpha |k|^2} \quad (3)$$

where T is the glass transition temperature, α is the surface tension in the transition, and k is the counterdirectional wave vector. The lower cut-off wavevector is $\sqrt{gd/\alpha}$, where d is the glass density. Now, the surface roughness can be defined in terms of roughness variance and power density

$$\sigma^2 = \frac{1}{2\pi^2} \int_{-\infty}^{\infty} P(k) d^2k \quad (4)$$

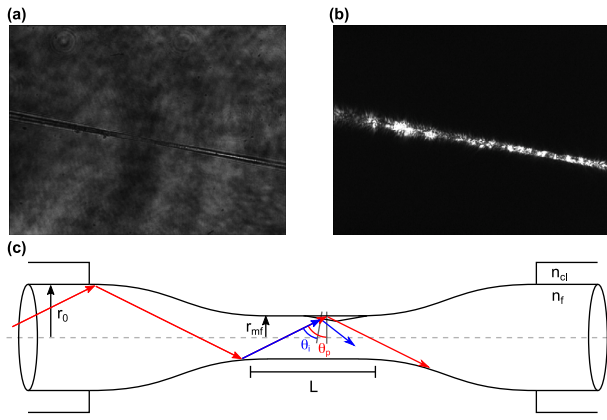


Fig. 4. In-house x100 optical microscope image of fabricated microfiber illuminated with (a) external light source and (b) guided light in the fiber itself while the external light source was switched off. (c) Model diagram of ray propagation inside the core of optical microfiber. The red arrow shows the ray bounced in between the smooth fiber walls. θ_p is the angle with fiber boundary for microfiber with continuous smooth boundary while the blue arrow shows the ray bounced in between the rough fiber walls (θ_i). (For interpretation of the references to color in this figure legend, the reader is referred to the web version of this article.)

In the single mode operation of the glass microfiber, the spectral components $P(k)$ are considerably large and therefore, they are responsible to enlarge the evanescent fields, which in turn contribute to the surface sensitivity of our device.

The surface roughness of the microfiber has a significant influence on the evanescent field. For smooth fiber, the wave propagates in θ_p due to the effect of total internal reflection (TIR). However, in case of rough fiber, the angle at which the ray hits the fiber boundary is different than the propagating angle (Fig. 4c). The boundary incident angle θ_i is influenced by the roughness of the surface and is defined as Zhong et al. (2013):

$$\theta_i = \theta_p - \tan^{-1}\left(\frac{2\delta}{\Delta}\right) \quad (5)$$

where θ_p is the propagating angle for smooth fiber with continuous boundary, δ is the average pit depth, and Δ is the average pit diameter as shown in Fig. 4c.

Eq. (5) shows that the incident angle θ_i is a function of fiber roughness. In addition, the change in θ_i has an influence on the penetration depth d_p of the evanescent field into the cellular medium as it is defined in Eq. (6) as the distance for which the field intensity decays to 37% ($1/e$) compared to the field intensity at the guiding layer boundary. The penetration depth is defined as:

$$d_p = \frac{\lambda}{2\pi\sqrt{n_f^2 \sin^2(\theta_i) - n_a^2}} \quad (6)$$

where n_a is the refractive index for the analyte, n_f is the refractive index for the fiber and θ_i is the incident angle. Eq. (6) emphasizes that the penetration depth depends on the incident angle. The smaller the incident angle, the larger the penetration of the evanescent field into the cellular medium which, in turn, improves the sensitivity of the device.

4. Conclusions

We found that the treatment of tumor cells with GDC0032, a beta-sparing PI3K, induced both growth arrest and altered the spectral lines in a dose-dependent manner. We interpreted the observed effect in terms of the roughness-induced absorption of light mediated by surface scatterers. Enhancement in absorption as high as 4 times was observed as compared to the theoretical estimations. This remarkable enhancement is interpreted by means of the roughness-induced absorption

resulting in increased interaction length due to the microfiber surface roughness. We explained the role of the surface roughness in the observed spectral effect. The monitoring method for treatment efficiency of ovarian cancer based on a microfiber device demonstrated here has several advantages compared to the conventional techniques involving the positron emission tomography (PET) and an X-ray computed tomography (CT). Importantly, the guided-light microfiber device does not involve irradiation of the patient, it is suitable for bedside applications, and gives real-time spectral response. Our findings form an essential step toward the development of early detection of response to cancer therapy. The simplicity of our approach opens a window for further in-vitro clinical investigation also for many accessible cancers such as esophageal, colorectal, cervical. In the future we aim at developing this system for in-vivo applications also suitable for lower acceptable such as brain cancers. This will consist the engineered biocompatible cage-jacket encapsulating fragile sensing area to monitor tumors in-vivo.

Declaration of competing interest

The authors declare that they have no known competing financial interests or personal relationships that could have appeared to influence the work reported in this paper.

CRedit authorship contribution statement

Aviad Katiyi: Investigation, Visualization, Methodology. **Jonathan Zorea:** Investigation, Resources. **Aviran Halstuch:** Investigation, Resources. **Moshe Elkabets:** Investigation, Supervision. **Alina Karabchevsky:** Investigation, Supervision, Conceptualization.

Acknowledgments

The research leading to these results was funded by the Health-Engineering multidisciplinary program by the Ben-Gurion University of the Negev, Israel, Israel Science Foundation (700/16), and the Concern Foundation, Israel #7895. J.Z. is acknowledging the support of the multidisciplinary fellowship (BGU), Israel. A.K., J.Z. and A.H. acknowledge the support of the Negev Fellowship (BGU), Israel. A. H. acknowledges the support from Israel Ministry of Science and Technology (3–14289).

References

- Abbas, T., Dutta, A., 2009. P21 in cancer: intricate networks and multiple activities. *Nat. Rev. Cancer* 9 (400).
- Agrawal, G.P., 2012. *Fiber-Optic Communication Systems*, vol. 222. John Wiley & Sons.
- Arumugam, M., 2001. Optical fiber communication—an overview. *Pramana* 57, 849–869.
- Bénard, J., D. Silva, J., D. Blois, M.C., Boyer, P., Duvillard, P., Chiric, E., Riou, G., 1985. Characterization of a human ovarian adenocarcinoma line, igrov1, in tissue culture and in nude mice. *Cancer Res.* 45, 4970–4979.
- Beyer, T., Townsend, D.W., Brun, T., Kinahan, P.E., Charron, M., Roddy, R., Jerin, J., Young, J., Byars, L., Nutt, R., et al., 2000. A combined pet/ct scanner for clinical oncology. *J. Nucl. Med.* 41, 1369–1379.
- Borovkova, O., Ignatyeva, D., Sekatskii, S., Karabchevsky, A., Belotelov, V., 2019. High-q surface electromagnetic wave resonance excitation in magneto-photonics crystals for super-sensitive detection of weak light absorption in near-ir. *ArXiv preprint arXiv:1910.11406*.
- Borovkova, O., Ignatyeva, D., Sekatskii, S., Karabchevsky, A., Belotelov, V., 2020. High-q surface electromagnetic wave resonance excitation in magnetophotonic crystals for supersensitive detection of weak light absorption in the near-infrared. *Photonics Res.* 8, 57–64.
- Caucheteur, C., Guo, T., Liu, F., Guan, B.O., Albert, J., 2016. Ultrasensitive plasmonic sensing in air using optical fibre spectral combs. *Nat. Commun.* 7 (13371).
- Chang, S.K., Mirabal, Y.N., Atkinson, E.N., Cox, D.D., Malpica, A., Follen, M., Richards-Kortum, R.R., 2005. Combined reflectance and fluorescence spectroscopy for in vivo detection of cervical pre-cancer. *J. Biomed. Opt.* 10, 024031.
- Chow, D.M., Yang, Z., Soto, M.A., Thévenaz, L., 2018. Distributed forward brillouin sensor based on local light phase recovery. *Nat. Commun.* 9 (2990).

- Dadadzhanov, D.R., Vartanyan, T.A., Karabchevsky, A., 2018. Vibrational overtones spectroscopy enabled by plasmonic nanoantennas. In: *Plasmonics: Design, Materials, Fabrication, Characterization, and Applications XVI*. International Society for Optics and Photonics, p. 107222E.
- Dadadzhanov, D.R., Vartanyan, T.A., Karabchevsky, A., 2019. Differential extinction of vibrational molecular overtone transitions with gold nanorods and its role in surface enhanced near-ir absorption (senira). *Opt. Express* 27, 29471–29478.
- Fischer, B., Lassen, U., Mortensen, J., Larsen, S., Loft, A., Bertelsen, A., Ravn, J., Clemenssen, P., Hogholm, K., et al., 2009. Preoperative staging of lung cancer with combined pet-ct. *New Engl. J. Med.* 361, 32–39.
- Fishman, D.A., Bozorgi, K., 2002. The scientific basis of early detection of epithelial ovarian cancer: the national ovarian cancer early detection program (nocepd). In: *Ovarian Cancer*. Springer, pp. 3–28.
- Fried, N.M., Irby, P.B., 2018. Advances in laser technology and fibre-optic delivery systems in lithotripsy. *Nat. Rev. Urol.* 15, 563–573.
- Geisler, T., Dohmen, L., Lenting, C., Fritzsche, M.B., 2019. Real-time in situ observations of reaction and transport phenomena during silicate glass corrosion by fluid-cell raman spectroscopy. *Nat. Mater.* 18 (342).
- Jackle, J., Kawasaki, K., 1995. Intrinsic roughness of glass surfaces. *J. Phys.: Condens. Matter* 7 (4351).
- Johnson, P., Federico, M., Kirkwood, A., Fosså, A., Berkahn, L., Carella, A., d'Amore, F., Enblad, G., Franceschetto, A., Fulham, M., et al., 2016. Adapted treatment guided by interim pet-ct scan in advanced hodgkin's lymphoma. *New Engl. J. Med.* 374, 2419–2429.
- Karabchevsky, A., Katiyi, A., Bin Abdul Khudus, M.I.M., Kavokin, A.V., 2018. Tuning the near-infrared absorption of aromatic amines on tapered fibers sculptured with gold nanoparticles. *ACS Photonics* 5, 2200–2207.
- Karabchevsky, A., Kavokin, A., 2016. Giant absorption of light by molecular vibrations on a chip. *Sci. Rep.* 6 (21201).
- Karabchevsky, A., Shalabney, A., 2016. Strong interaction of molecular vibrational overtones with near-guided surface plasmon polariton. In: *Optical Sensing and Detection IV*. International Society for Optics and Photonics, p. 98991T.
- Katiyi, A., Karabchevsky, A., 2017. Figure of merit of all-dielectric waveguide structures for absorption overtone spectroscopy. *J. Lightwave Technol.* 35, 2902–2908.
- Katiyi, A., Karabchevsky, A., 2018. Si nanostrip optical waveguide for on-chip broadband molecular overtone spectroscopy in near-infrared. *ACS Sensors* 3, 618–623.
- Kotz, F., Arnold, K., Bauer, W., Schild, D., Keller, N., Sachsenheimer, K., Nargang, T.M., Richter, C., Helmer, D., Rapp, B.E., 2017. Three-dimensional printing of transparent fused silica glass. *Nature* 544 (337).
- Kurian, A.W., Sigal, B.M., Plevritis, S.K., 2010. Survival analysis of cancer risk reduction strategies for brca1/2 mutation carriers. *J. Clin. Oncol.* 28, 222.
- Lee, J., Ledermann, J., Kohn, E., 2013. Parp inhibitors for brca1/2 mutation-associated and brca-like malignancies. *Ann. Oncol.* 25, 32–40.
- Lengyel, E., 2010. Ovarian cancer development and metastasis. *Am. J. Pathol.* 177, 1053–1064.
- Lorenzo, J.R., 2012. *Principles of Diffuse Light Propagation: Light Propagation in Tissues with Applications in Biology and Medicine*. World Scientific.
- Mackanos, M.A., Contag, C.H., 2010. Fiber-optic probes enable cancer detection with ftr spectroscopy. *Trends Biotechnol.* 28, 317–323.
- Mahadevan-Jansen, A., Mitchell, M.F., Ramanujam, N., Utzinger, U., Richards-Kortum, R., 1998. Development of a fiber optic probe to measure nir raman spectra of cervical tissue in vivo. *Photochem. Photobiol.* 68, 427–431.
- Midwinter, J., 1976. Trends in optical fibre transmission research. *Nature* 261 (371).
- Motz, J.T., Hunter, M., Galindo, L.H., Gardecki, J.A., Kramer, J.R., Dasari, R.R., Feld, M.S., 2004. Optical fiber probe for biomedical raman spectroscopy. *Appl. Opt.* 43, 542–554.
- Noone, A., Howlander, N., Krapcho, M., Miller, D., Brest, A., Yu, M., Ruhl, J., et al., 2018. *Seer Cancer Statistics Review, 1975–2015, Based on November 2017 Seer Data Submission*. Posted To the Seer Web Site, April 2018. National Cancer Institute, Bethesda, MD.
- Okoshi, T., 1987. Recent advances in coherent optical fiber communication systems. *J. Lightwave Technol.* 5, 44–52.
- Paget, R., 1924. Fused silica.
- Palais, J.C., 1988. *Fiber Optic Communications*. Prentice Hall, Englewood Cliffs.
- Pelosi, E., Messa, C., Sironi, S., Picchio, M., Landoni, C., Bettinardi, V., Gianolli, L., De Maschio, A., Gilardi, M.C., Fazio, F., 2004. Value of integrated pet/ct for lesion localisation in cancer patients: a comparative study. *Eur. J. Nucl. Med. Mol. Imaging* 31, 932–939.
- Peterson, J.I., Vurek, G.G., 1984. Fiber-optic sensors for biomedical applications. *Science* 224, 123–127.
- Rao, Y.J., Webb, D.J., Jackson, D.A., Zhang, L., Bennion, I., 1997. In-fiber bragg-grating temperature sensor system for medical applications. *J. Lightwave Technol.* 15, 779–785.
- Rao, Y.J., Webb, D., Jackson, D.A., Zhang, L., Bennion, I., 1998. Optical in-fiber bragg grating sensor systems for medical applications.
- Schäfers, K.P., Stegger, L., 2008. Combined imaging of molecular function and morphology with pet/ct and spect/ct: image fusion and motion correction. *Basic Res. Cardiol.* 103, 191–199.
- Shamkhi, H.K., Baryshnikova, K.V., Sayanskiy, A., Kapitanova, P., Terekhov, P.D., Belov, P., Karabchevsky, A., Evlyukhin, A.B., Kivshar, Y., Shalin, A.S., 2019. Transverse scattering and generalized kerker effects in all-dielectric mie-resonant metaoptics. *Phys. Rev. Lett.* 122, 193905.
- Soto, M.A., Ramirez, J.A., Thevenaz, L., 2016. Intensifying the response of distributed optical fibre sensors using 2d and 3d image restoration. *Nat. Commun.* 7 (10870).
- Stegger, L., Juergens, K.U., Kliesch, S., Wormanns, D., Weckesser, M., 2007. Unexpected finding of elevated glucose uptake in fibrous dysplasia mimicking malignancy: contradicting metabolism and morphology in combined pet/ct. *Eur. Radiol.* 17 (1784).
- Struve, W.S., 1989. *Fundamentals of Molecular Spectroscopy*. Wiley, New York.
- Suart, B., 2004. *Infrared Spectroscopy: Fundamental and Applications*. John Wiley & Sons, Ltd.
- Suematsu, Y., 1983. Long-wavelength optical fiber communication. *Proc. IEEE* 71, 692–721.
- Sung, K.B., Richards-Kortum, R., Follen, M., Malpica, A., Liang, C., Descour, M.R., 2003. Fiber optic confocal reflectance microscopy: a new real-time technique to view nuclear morphology in cervical squamous epithelium in vivo. *Opt. Express* 11, 3171–3181.
- Terekhov, P.D., Babicheva, V.E., Baryshnikova, K.V., Shalin, A.S., Karabchevsky, A., Evlyukhin, A.B., 2019a. Multipole analysis of dielectric metasurfaces composed of nonspherical nanoparticles and lattice invisibility effect. *Phys. Rev. B* 99, 045424.
- Terekhov, P.D., Baryshnikova, K.V., Artemyev, Y.A., Karabchevsky, A., Shalin, A.S., Evlyukhin, A.B., 2017. Multipolar response of nonspherical silicon nanoparticles in the visible and near-infrared spectral ranges. *Phys. Rev. B* 96, 035443.
- Terekhov, P.D., Baryshnikova, K.V., Greenberg, Y., Fu, Y.H., Evlyukhin, A.B., Shalin, A.S., Karabchevsky, A., 2019b. Enhanced absorption in all-dielectric metasurfaces due to magnetic dipole excitation. *Sci. Rep.* 9 (3438).
- Terekhov, P., Shamkhi, H., Gurvitz, E., Baryshnikova, K., Evlyukhin, A., Shalin, A., Karabchevsky, A., 2019c. Broadband forward scattering from dielectric cubic nanoantenna in lossless media. *Opt. Express* 27, 10924–10935.
- Wan, N.H., Meng, F., Schröder, T., Shiue, R.J., Chen, E.H., Englund, D., 2015. High-resolution optical spectroscopy using multimode interference in a compact tapered fibre. *Natu. Commun.* 6 (7762).
- Wheeler, O.H., 1959. Near infrared spectra of organic compounds. *Chem. Rev.* 59, 629–666.
- Zhong, N., Zhu, X., Liao, Q., Wang, Y., Chen, R., Sun, Y., 2013. Effects of surface roughness on optical properties and sensitivity of fiber-optic evanescent wave sensors. *Appl. Opt.* 52, 3937–3945.
- Zorea, J., Prasad, M., Cohen, L., Li, N., Schefzik, R., Ghosh, S., Rotblat, B., Brors, B., Elkabets, M., 2018. Igf1r upregulation confers resistance to isoform-specific inhibitors of pi3k in pi3ka-driven ovarian cancer. *Cell Death Dis.* 9 (944).

3 Additional studies

3.1 Scattering pattern of a cylindrical inclusion on a waveguide

For understanding the behavior of inclusions on the mode in a waveguide, I numerically investigated the influence of a single cylindrical inclusion with different diameters in a silicon nitride ridge waveguide on the scattering pattern [51]. I investigated the influence of a single inclusion by numerical simulation with COMSOL multiphysics. A single cylindrical inclusion was placed in a ridge waveguide made of silicon-nitride (Si_3N_4) with a width of $1 \mu\text{m}$, height of $0.8 \mu\text{m}$ and wavelength of $1.55 \mu\text{m}$ as shown in Fig. 10. The refractive indices for silica substrate and silicon nitride guiding layer were $n_{\text{sub}} = 1.444$ and $n_{\text{wg}} = 1.997$, respectively. The fundamental TE mode was launched inside the waveguide as shown in Fig. 10.

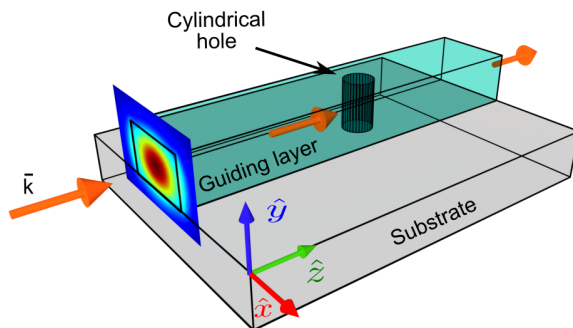


Figure 10: Illustration of the waveguide with cylindrical inclusion through the guiding layer [51].

I calculated the angular diagrams of electric dipole (eDip), electric quadrupole (eQuad) and magnetic dipole (mDip) moments normalized to the maximum while varying the diameter of the inclusion for $D = \lambda/5, \lambda/10, \lambda/20, \lambda/100$ in xy and yz planes when the cylinder is in the middle of each plane.

Figure 11 shows the angular diagrams of multipole emitted power from inclusion (cylindrical cavities) for $D = \lambda/5, \lambda/10, \lambda/20, \lambda/100$. The blue curve shows the angular diagram in yz plane, and the red curve shows the angular diagram in xy plane. While narrowing the hole, the electric dipole becomes dominant. The maxima are changed when the diameter of the inclusion gets smaller. For a relatively large inclusion diameter, the incident field on the cylinder is comprised of the propagating modes in the waveguides as well as the reflections from the scattered fields. As the diameter becomes smaller, the scattered fields decrease, while the propagating modes do not experience a change. The scattered field pattern becomes more similar to the fundamental electric and magnetic multipoles. For example, figure 12 shows the evolution in the scattered field pattern for the magnetic dipole for different hole

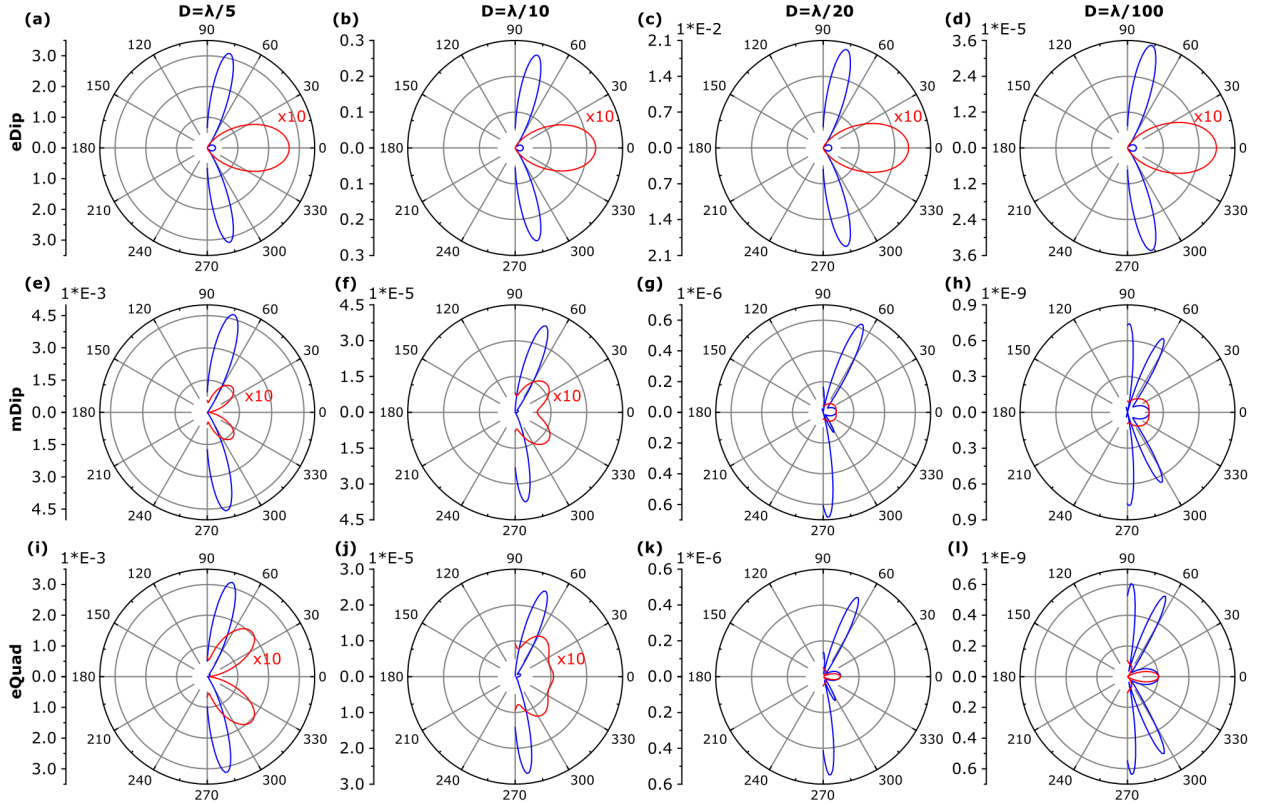


Figure 11: Angular diagrams for $D = \lambda/(5, 10, 20, 100)$ (different diameter from each column as labeled above the columns) for fundamental TE. Some of the fields at xy plane in the polar graph are multiplied by 10 for comparison. The blue curve shows the angular diagram in yz plane and the red curve shows the angular diagram in xy plane, respectively. The 1st row shows the electric dipole (eDip), the 2nd row shows the magnetic dipole (mDip), and the 3rd row shows the electric quadrupole (eQuad) - as labeled in the y-axis of (a,e,i) (adapted from [51]).

diameters.

From these results, I concluded that the scattered field from inclusion can be utilized for transferring power to high-order modes, enhancing the evanescent field. In addition, a larger diameter has a stronger influence on the scattering pattern.

3.2 Subwavelength grating on a waveguide for enhanced sensitivity

As I found in the microfiber experiment that the random roughness of the microfiber surface enhances the sensitivity of the microfiber, I proceeded to study the influence of constant roughness on sensitivity. Using a designed structure as constant roughness will allow the modification of a structure needed for the sensing application. For the constant roughness,

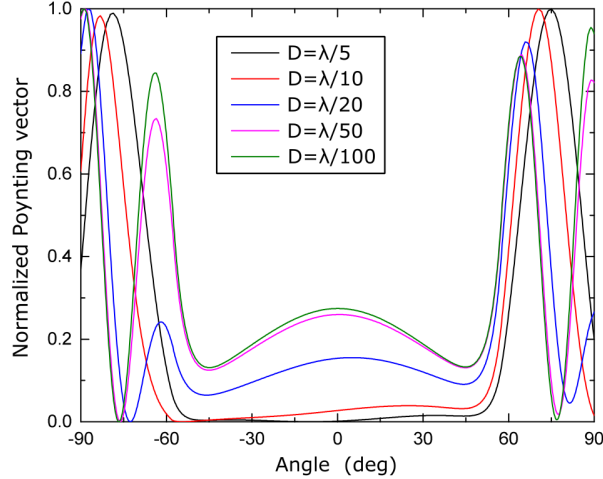


Figure 12: Calculated magnetic dipole for $D = \lambda/(5, 10, 20, 50, 100)$ presented in Cartesian coordinates plot (adapted from [51]).

I used a subwavelength grating on top of a multimode silicon rib waveguide, as illustrated in Fig. 13.

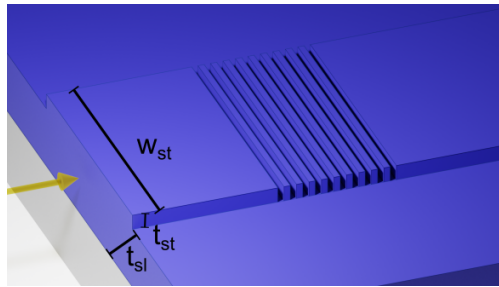


Figure 13: Illustration of the waveguide with the subwavelength grating.

A numerical simulation was performed to check the influence of the grating on the evanescent field. Using Lumerical FDTD, I built a rib silicon waveguide with length of $20 \mu\text{m}$, slab thickness (t_{sl}) of $1.6 \mu\text{m}$, strip thickness (t_{st}) of $0.4 \mu\text{m}$ and width (w_{st}) of $6 \mu\text{m}$ (see Fig. 13 for the dimensions). A subwavelength grating with a period of 400 nm , a duty cycle of 50% , depth of 400 nm and length of $10 \mu\text{m}$ was placed in the middle of the waveguide. These dimensions were chosen due to the fabrication limitation of the focused ion beam (FIB) machine. To test the influence on the evanescent field, I measured the field 50 nm above the top facet. Figure 14 shows the electric field of the fundamental transverse electric (TE) mode at a distance of 50 nm from the top facet for the two cases.

Figure 14a shows that the normalized electric field for untouched rib waveguide is around 0.05 . Figure 14b shows the field for a rib waveguide with the subwavelength grating. It shows

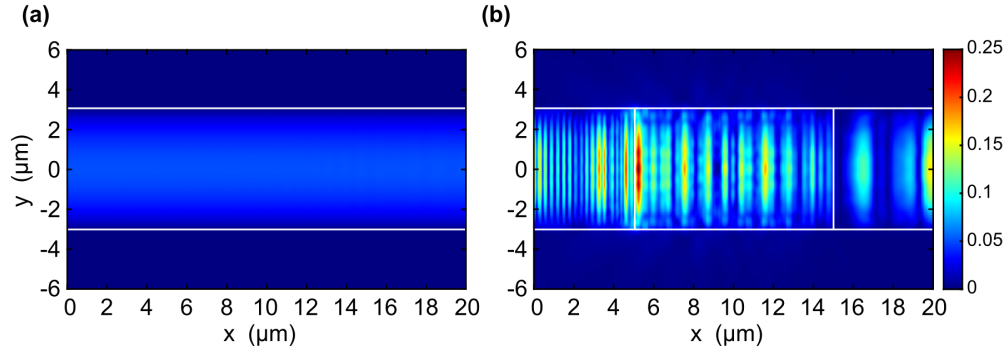


Figure 14: The normalized electric field of the fundamental transverse electric (TE) mode in distance of 50 nm from the top facet for (a) untouched rib silicon waveguide and (b) rib silicon waveguide with subwavelength grating.

an increase in the evanescent field compared to a waveguide without the subwavelength grating. To check the simulated structure, I fabricated a subwavelength grating on an SOI rib waveguide. Using a focused ion beam machine, I milled a subwavelength grating with a period of 400 nm, a duty cycle of 50%, depth of 400 nm and total length of 16 μm . A scanning electron microscope (SEM) image of the fabricated subwavelength grating is shown in Fig. 15.

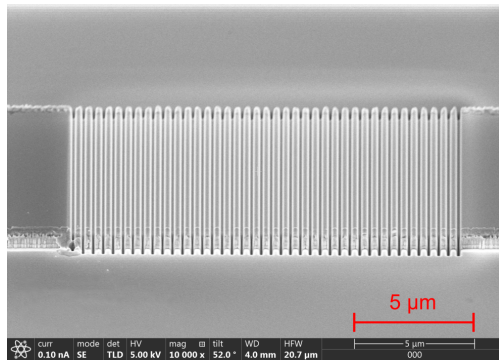


Figure 15: Scanning electron microscope (SEM) image of the fabricated subwavelength grating on the waveguide.

Next, I built an experimental setup, as shown in Fig. 16a, to study the waveguide with the grating. A broadband laser was coupled to a single-mode fiber using an x40 objective. The single-mode fiber was connected to a lensed fiber that was coupled to the waveguide. The waveguide output was collected to an optical spectrum analyzer by a fiber. The setup was monitored by a microscope for precise alignment of the input and output fibers.

The influence of the subwavelength grating on the absorption of *N*-Methylaniline was tested: First, by checking the transmission for untouched clean waveguide. Next, by dripping 3 μl of *N*-Methylaniline on the waveguide and measuring the transmission. Then, by moving

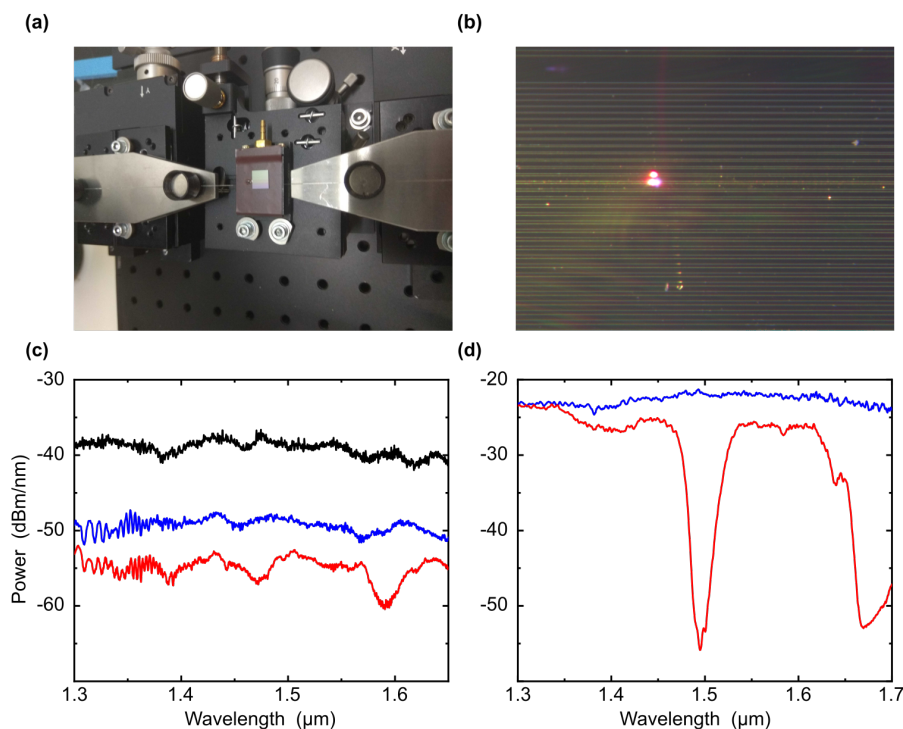


Figure 16: (a) Laser to waveguide coupling setup. (b) Scattering from the grating. (c) The measured transmission of a clean untouched waveguide (black curve), untouched waveguide with *N*-Methylaniline (blue curve) and waveguide with milled subwavelength grating and *N*-Methylaniline (red curve). (d) Transmission of *N*-Methylaniline in 1 cm cuvette.

the laser to the waveguide with the subwavelength grating. Figure 16b shows the top view of the illuminated waveguide with the subwavelength grating. It shows the scattering caused by the grating. The results of this experiment are shown in Fig. 16c, indicating that when *N*-Methylaniline was dripped on an untouched waveguide (blue curve), the absorption was very low. When a waveguide with the subwavelength grating and *N*-Methylaniline was checked, the absorption was enhanced and was clearly seen (red curve). The absorption of the N-H bond can be seen around 1475 nm and the absorption of C-H around 1600 nm. To verify, I checked *N*-Methylaniline in a 1 cm cuvette (Fig. 16d). I observed a shift in the absorption between the *N*-Methylaniline in the cuvette (Fig. 16d) and *N*-Methylaniline on a waveguide (Fig. 16c).

From these results, I concluded that constant roughness can be used for enhancing the sensitivity of the sensor.

4 Conclusions and Discussion

To summarize, I investigated guided wave architectures for overtone spectroscopy.

First, I investigated the overtone absorption on a multimode silicon-on-insulator rib waveguide. As the order of the mode increases, the evanescent field is enhanced, which in turn improves the sensitivity. The multimode behavior of a multimode SOI waveguide enhanced the sensitivity in three orders of magnitude by launching power to high order modes. A precise distinction was observed between two similar organic molecules, aniline and *N*-methylaniline (aniline derivative) and a CH bond second overtone without any surface modification on the waveguide was identified through scanning over the absorption dips in the NIR transmission spectra. Another method for transferring power to high order mode is by deflecting the Talbot effect using perturbations of cylindrical shape in a multimode waveguide core. The deflected Talbot effect, due to a cluster of inclusions milled into a waveguide, enhanced the absorption of molecular transition overtones of weakly absorbing *N*-methylaniline. The absorption line of the N-H bond of *N*-methylaniline around 1.5 μm experienced a drop of 3.5 dB as compared to an unperturbed waveguide.

Further research was performed on the influence of the diameter of a single inclusion in a silicon nitride ridge waveguide on the scattering pattern. I found that changing the geometry of the inclusion affects the directional scattering effect. When the hole diameter is comparable to the incident wavelength, the absorption is enhanced and it can be used for sensing. As the radius becomes smaller, the fundamental electric and magnetic multipoles become dominant and can be used for single-photon source applications on a chip. Therefore, the diameter of inclusion can be modified and utilized for chemical analytes, quantum dots, nanolasers and others.

Next, I studied another method for enhancing the sensitivity of the overtone absorption by changing the confinement of the mode. Decreasing the confinement of the mode increases the evanescent field, which in turn enhances the sensitivity. The interaction between the evanescent fields of microfiber and ovarian cancer intercellular medium at different treatment concentrations was investigated. The microfiber was fabricated by tapering an optical fiber. I found that the spectral lines were altered in a dose-dependent manner. In addition, an enhancement in absorption as high as 4 times was observed, as compared to the theoretical estimations. This remarkable enhancement is interpreted by means of the roughness-induced absorption. Besides the enhancement caused by decreasing the mode confinement by tapering an optical fiber, I found that the random roughness of the microfiber enhances sensitivity, by further increasing the penetration depth of the evanescent field.

The enhancement in sensitivity can be also achieved by the fabrication of a designed

constant roughness on the surface of the waveguide, for example a grating. Surface roughness can be used for enhancing the sensitivity and modulated accordingly.

4.1 Future research and perspectives

Enhancing the sensitivity by decreasing the mode confinement, which I explored during my research, can be studied in the direction of tapering the guiding layer of a waveguide. Waveguides have advantages over conventional tapered fibers. The main advantage is that waveguides are more robust and the modification of waveguides is easier, which allows their design for specific applications. Further investigation can be performed on combining the effect of tapering with the enhancement due to surface roughness, a feature that can be used for medical and sensing applications such as creating lab on a chip by adding laser source on the chip, or for medical applications by monitoring treatment efficiency.

References

- [1] Aviad Katiyi and Alina Karabchevsky. Figure of merit of all-dielectric waveguide structures for absorption overtone spectroscopy. *Journal of Lightwave Technology*, 35(14):2902–2908, 2017.
- [2] Alina Karabchevsky, Aviad Katiyi, Angeleene S Ang, and Adir Hazan. On-chip nanophotonics and future challenges. *Nanophotonics*, 9(12):3733–3753, 2020.
- [3] KC Kao and George A Hockham. Dielectric-fibre surface waveguides for optical frequencies. In *Proceedings of the Institution of Electrical Engineers*, volume 113, pages 1151–1158. IET, 1966.
- [4] AF Evans, DG Hall, and WP Maszara. Propagation loss measurements in silicon-on-insulator optical waveguides formed by the bond-and-etchback process. *Applied physics letters*, 59(14):1667–1669, 1991.
- [5] GT Reed, Li Jinhua, CK Tang, Lin Chenglu, PLF Hemment, and AG Rickman. Silicon on insulator optical waveguides formed by direct wafer bonding. *Materials Science and Engineering: B*, 15(2):156–159, 1992.
- [6] Mahmoud M Abouelhell and Fred J Leonberger. Waveguides in lithium niobate. *Journal of the American Ceramic Society*, 72(8):1311–1321, 1989.
- [7] Cheng Wang, Mian Zhang, Brian Stern, Michal Lipson, and Marko Lončar. Nanophotonic lithium niobate electro-optic modulators. *Optics express*, 26(2):1547–1555, 2018.
- [8] Cheng Wang, Mian Zhang, Xi Chen, Maxime Bertrand, Amirhassan Shams-Ansari, Sethumadhavan Chandrasekhar, Peter Winzer, and Marko Lončar. Integrated lithium niobate electro-optic modulators operating at cmos-compatible voltages. *Nature*, 562(7725):101–104, 2018.
- [9] Lin Chang, Andreas Boes, Xiaowen Guo, Daryl T Spencer, MJ Kennedy, Jon D Peters, Nicolas Volet, Jeff Chiles, Abijith Kowligy, Nima Nader, et al. Heterogeneously integrated gaas waveguides on insulator for efficient frequency conversion. *Laser & Photonics Reviews*, 12(10):1800149, 2018.
- [10] Oliver Kahl, Simone Ferrari, Vadim Kovalyuk, Gregory N Goltsman, Alexander Korneev, and Wolfram HP Pernice. Waveguide integrated superconducting single-photon detectors with high internal quantum efficiency at telecom wavelengths. *Scientific reports*, 5(1):1–11, 2015.

- [11] Max Born and Emil Wolf. *Principles of Optics: Electromagnetic Theory of Propagation, Interference and Diffraction of Light*. Elsevier, 2013.
- [12] Arnab Dewanjee, J Stewart Aitchison, and Mo Mojahedi. Experimental demonstration of a high efficiency compact bilayer inverse taper edge coupler for si photonics. In *2016 IEEE Photonics Conference (IPC)*, pages 414–415. IEEE, 2016.
- [13] Afshin Ghaffari, Mehrdad Djavid, and Mohammad Sadegh Abrishamian. Power splitters with different output power levels based on directional coupling. *Applied optics*, 48(8):1606–1609, 2009.
- [14] Hirohito Yamada, Tao Chu, Satomi Ishida, and Yasuhiko Arakawa. Optical directional coupler based on si-wire waveguides. *IEEE photonics technology letters*, 17(3):585–587, 2005.
- [15] Zeqin Lu, Han Yun, Yun Wang, Zhitian Chen, Fan Zhang, Nicolas AF Jaeger, and Lukas Chrostowski. Broadband silicon photonic directional coupler using asymmetric-waveguide based phase control. *Optics express*, 23(3):3795–3808, 2015.
- [16] Tatsuro Hiraki, Takuma Aihara, Koichi Hasebe, Koji Takeda, Takuro Fujii, Takaaki Kakitsuka, Tai Tsuchizawa, Hiroshi Fukuda, and Shinji Matsuo. Heterogeneously integrated iii–v/si mos capacitor mach–zehnder modulator. *Nature Photonics*, 11(8):482–485, 2017.
- [17] Guoliang Li, Ashok V Krishnamoorthy, Ivan Shubin, Jin Yao, Ying Luo, Hiren Thacker, Xuezhe Zheng, Kannan Raj, and John E Cunningham. Ring resonator modulators in silicon for interchip photonic links. *IEEE Journal of Selected Topics in Quantum Electronics*, 19(6):95–113, 2013.
- [18] Jörn P Epping, Tim Hellwig, Marcel Hoekman, Richard Mateman, Arne Leinse, René G Heideman, Albert van Rees, Peter JM van der Slot, Chris J Lee, Carsten Fallnich, et al. On-chip visible-to-infrared supercontinuum generation with more than 495 thz spectral bandwidth. *Optics express*, 23(15):19596–19604, 2015.
- [19] Xing Liu, Minhao Pu, Binbin Zhou, Clemens J Krückel, Attila Fülöp, Morten Bache, et al. Octave-spanning supercontinuum generation in a silicon-rich nitride waveguide. *Optics letters*, 41(12):2719–2722, 2016.
- [20] Walter S Struve. *Fundamentals of molecular spectroscopy*. Wiley New York, 1989.

- [21] Qian Wang and Gerald Farrell. All-fiber multimode-interference-based refractometer sensor: proposal and design. *Optics letters*, 31(3):317–319, 2006.
- [22] Kerstin Schroeder, Wolfgang Ecke, Rudolf Mueller, Reinhardt Willsch, and Andrey Andreev. A fibre bragg grating refractometer. *Measurement Science and technology*, 12(7):757, 2001.
- [23] Jože Grdadolnik. Atr-ftir spectroscopy: Its advantage and limitations. *Acta Chimica Slovenica*, 49(3):631–642, 2002.
- [24] Wim Bogaerts, Peter De Heyn, Thomas Van Vaerenbergh, Katrien De Vos, Shankar Kumar Selvaraja, Tom Claes, Pieter Dumon, Peter Bienstman, Dries Van Thourhout, and Roel Baets. Silicon microring resonators. *Laser & Photonics Reviews*, 6(1):47–73, 2012.
- [25] Arthur Nitkowski, Long Chen, and Michal Lipson. Cavity-enhanced on-chip absorption spectroscopy using microring resonators. *Optics express*, 16(16):11930–11936, 2008.
- [26] Juejun Hu, Vladimir Tarasov, Anu Agarwal, Lionel Kimerling, Nathan Carlie, Laetitia Petit, and Kathleen Richardson. Fabrication and testing of planar chalcogenide waveguide integrated microfluidic sensor. *Optics Express*, 15(5):2307–2314, 2007.
- [27] A Karabchevsky and AV Kavokin. Giant absorption of light by molecular vibrations on a chip. *Scientific reports*, 6(1):1–7, 2016.
- [28] Antoine Gervais, Philippe Jean, Wei Shi, and Sophie LaRochelle. Design of slow-light subwavelength grating waveguides for enhanced on-chip methane sensing by absorption spectroscopy. *IEEE Journal of Selected Topics in Quantum Electronics*, 25(3):1–8, 2018.
- [29] Alina Karabchevsky. Integrated photonics course. University Lecture, 2020.
- [30] Robert G Hunsperger. *Integrated optics*, volume 4. Springer, 1995.
- [31] Peter W Atkins and Ronald S Friedman. *Molecular quantum mechanics*. Oxford university press, 2011.
- [32] Aviad Katiyi and Alina Karabchevsky. Si nanostrip optical waveguide for on-chip broadband molecular overtone spectroscopy in near-infrared. *ACS sensors*, 3(3):618–623, 2018.

- [33] S Shaji and TMA Rasheed. Vibrational overtone spectra of chloroanilines - evidence for intramolecular hydrogen bonding in o-chloroaniline. *Spectrochimica Acta Part A: Molecular and Biomolecular Spectroscopy*, 57(2):337–347, 2001.
- [34] Kane Yee. Numerical solution of initial boundary value problems involving maxwell's equations in isotropic media. *IEEE Transactions on antennas and propagation*, 14(3):302–307, 1966.
- [35] Alexander Hrennikoff. Solution of problems of elasticity by the framework method. 1941.
- [36] Gilberto Brambilla. Optical fibre nanowires and microwires: a review. *Journal of Optics*, 12(4):043001, 2010.
- [37] Cynthia A Volkert and Andrew M Minor. Focused ion beam microscopy and micromachining. *MRS bulletin*, 32(5):389–399, 2007.
- [38] Pavel D Terekhov, Kseniia V Baryshnikova, Yakov Greenberg, Yuan Hsing Fu, Andrey B Evlyukhin, Alexander S Shalin, and Alina Karabchevsky. Enhanced absorption in all-dielectric metasurfaces due to magnetic dipole excitation. *Scientific reports*, 9(1):1–9, 2019.
- [39] Eran Falek, Aviad Katiyi, Yakov Greenberg, and Alina Karabchevsky. On-chip metasurface-on-facets for ultra-high transmission through waveguides in near-infrared. *Advanced Optical Materials*, 9(11):2100130, 2021.
- [40] Zvi Rappoport. *The chemistry of anilines*, volume 169. John Wiley & Sons, 2007.
- [41] S Shaji, Shibu M Eappen, TMA Rasheed, and KPR Nair. NIR vibrational overtone spectra of *N*-methylaniline, *N,N*-dimethylaniline and *N,N*-diethylaniline - a conformational structural analysis using local mode model. *Spectrochimica Acta Part A: Molecular and Biomolecular Spectroscopy*, 60(1-2):351–355, 2004.
- [42] KB Whetsel, WE Roberson, and MW Krell. Near-infrared spectra of primary aromatic amines. *Analytical Chemistry*, 30(10):1598–1604, 1958.
- [43] Aviad Katiyi and Alina Karabchevsky. Deflected talbot-mediated overtone spectroscopy in near-infrared as a label-free sensor on a chip. *ACS sensors*, 5(6):1683–1688, 2020.
- [44] Lung-Wei Chung, San-Liang Lee, and Yen-Juei Lin. Principles and application of reduced beat length in mmi couplers. *Optics express*, 14(19):8753–8764, 2006.

- [45] Andrea Irace and Giovanni Breglio. All-silicon optical temperature sensor based on multi-mode interference. *Optics express*, 11(22):2807–2812, 2003.
- [46] Henry Fox Talbot. Lxxvi. facts relating to optical science. no. iv. *The London and Edinburgh Philosophical Magazine and Journal of Science*, 9(56):401–407, 1836.
- [47] Aviad Katiyi, Jonathan Zorea, Aviran Halstuch, Moshe Elkabets, and Alina Karabchevsky. Surface roughness-induced absorption acts as an ovarian cancer cells growth sensor-monitor. *Biosensors and Bioelectronics*, 161:112240, 2020.
- [48] David A Fishman and Kenny Bozorgi. The scientific basis of early detection of epithelial ovarian cancer: the national ovarian cancer early detection program (nocedp). In *Ovarian cancer*, pages 3–28. Springer, 2002.
- [49] Ernst Lengyel. Ovarian cancer development and metastasis. *The American journal of pathology*, 177(3):1053–1064, 2010.
- [50] Govind P Agrawal. *Fiber-optic communication systems*, volume 222. John Wiley & Sons, 2012.
- [51] Yuriy A Artemyev, Vassili Savinov, Aviad Katiyi, Alexander S Shalin, and Alina Karabchevsky. Non-isolated sources of electromagnetic radiation by multipole decomposition for photonic quantum technologies on a chip with nanoscale apertures. *Nanoscale Advances*, 3(1):190–197, 2020.

תקציר

אופטיקת מוליכי גל מספקת פלטפורמה רחבה למחקר פונדמנטאלי ויישומי במגוון של מערכות. זאת בשל העובדה כי למוליכי גל ישנן תכונות ייחודיות, כגון איפנון השדה הדועך, מזעור ובעיקר היכולת להיות מתוכננים בהתאם ליישום הנדרש. היכולת לחקור ויברציות מולקולריות בתדירות הבסיסית או בתדירויות גבוהות יותר (overtones) הינה מרכיב חשוב בטכניקות ניטור רפואי וחישה בכלל מכיוון שתדר האור הנבלע על ידי מולקולות מתאים בדיוק להפרשי הרמות הוויברציונית – טכניקות מבוססות על ספקטרוסקופיה מולקולרית מהווים דרך ישירה למדידה של הפרשי רמות אלו, מבנה מולקולרי של המולקולה דרך קשרים בין-אטומיים. ספקטרוסקופיה ויברציונית באינפרא-אדום הקרוב מבוססת על קשרי-גומלין בין אור לחומר והינה כלי רב עוצמה לחקר מבנים מולקולריים באינפרא-אדום הקרוב. אף על פי שתחום האינפרא-אדום הקרוב בעל פוטנציאל רב, הוא לא נחקר היטב בשל כמות האור הנמוכה הנבלעת על ידי המולקולה בתדרים גבוהים. הבנת מנגנון הבליעה של אופני תנודה בתדרים גבוהים יאפשר פיתוח שיטות גילוי חדשות, יעילות ונגישות היכולות לשמש למגוון יישומים כגון חיישנים כימיים ויישומים רפואיים כגון ניטור יעילות הטיפול בסרטן. במהלך המחקר של תואר שלישי, חקרתי אופני תנודה מולקולריים בתדרים גבוהים במגוון מערכות, הכוללות מולקולות שונות וארכיטקטורות שונות של מוליכי גל המפורטות בתזה.

המחקר שלי מתמקד בחקר מנגנון הבליעה על ידי מעברי רעידה מולקולריים הרמוניים בעזרת ארכיטקטורות של מוליכי גל אופטיים. מצאתי שניתן להשתמש במוליכי גל אופטיים לספקטרוסקופיה של רעידות הרמוניות. על ידי יצירת הפרעות/הפרעות בשכבה ההולכה, כגון חורים או סריג, ניתן לשפר את הרגישות של מוליך הגל. בנוסף, ניתן להקטין את הכליאה של האופן בתווך המוליך על ידי הכיווץ של סיב אופטי על מנת לשפר הרגישות, הנובעת מהגדלת עומק החדירה של השדה הדועך.

מוליכי גל אופטיים לישומי חישה

מחקר לשם מילוי חלקי של הדרישות לקבלת תואר "דוקטור לפילוסופיה"

מאת

קטיעי

אביעד

הוגש לסינאט אוניברסיטת בן גוריון בנגב

25/10/2021

י"ט חשוון תשפ"ב

באר שבע

מוליכי גל אופטיים לישומי חישה

מחקר לשם מילוי חלקי של הדרישות לקבלת תואר "דוקטור לפילוסופיה"

מאת

אביעד קטיעי

הוגש לסינאט אוניברסיטת בן גוריון בנגב

AK

אישור המנחה

אישור דיקן בית הספר ללימודי מחקר מתקדמים ע"ש קרייטמן

25/10/2021

י"ט חשוון תשפ"ב

באר שבע

העבודה נעשתה בהדרכת

פרופ' אלינה קרבצ'בסקי

במחלקה הנדסת אלקטרואופטיקה ופוטוניקה

בפקולטה למדעי ההנדסה

הצהרת תלמיד המחקר עם הגשת עבודת הדוקטור לשיפוט

אני החתום מטה מצהיר/ה בזאת: (אנא סמן):

חיברתי את חיבורי בעצמי, להוציא עזרת ההדרכה שקיבלתי מאת מנחה/ים.

החומר המדעי הנכלל בעבודה זו הינו פרי מחקרי מתקופת היותי תלמיד/ת מחקר.

____ בעבודה נכלל חומר מחקרי שהוא פרי שיתוף עם אחרים, למעט עזרה טכנית שאינה כוללת ניתוח תוצאות, הנהוגה בעבודה ניסיונית. לפי כך מצורפת בזאת הצהרה על תרומתי ותרומת שותפי למחקר, שאושרה על ידם ומוגשת בהסכמתם.

____ תזה במתכונת אסופת מאמרים, כוללת מאמרים בהם אני מחבר ראשון משותף (equal contribution). במקרה זה, נא לצרף הצהרה של המחבר השותף על חלקו בפרסום, ואישורו לכך, שמאמר זה לא יוכל להיכלל בתזת מאמרים נוספת, שהוא יגיש.

תאריך 25/10/2021 שם התלמיד/ה אביעד קטיעי חתימה אביעד קטיעי